LEVEL-SET SEGMENTATION OF BRAIN TUMORS IN MAGNETIC RESONANCE IMAGES

SIMA TAHERI

(B.Sc. and M.Sc., Sharif University of Technology, Iran)

A THESIS SUBMITTED

FOR THE DEGREE OF MASTER OF ENGINEERING

DEPARTMENT OF ELECTRICAL AND COMPUTER ENGINEERING

NATIONAL UNIVERSITY OF SINGAPORE

2007

To my husband and my parents...

who gave me their wonderful support...

Acknowledgements

I am truly grateful to my supervisor, Assoc. Prof. Sim Heng Ong, for his continuous guidance and support during this work. Without his guidance, this work would not be possible. I am also deeply indebted to the Agency for Science, Technology and Research (A*STAR) for the award of a research scholarship.

I am thankful to Assoc. Prof. Vincent Chong for his collaboration in this work and for the dataset he provided me with. I would also like to give thanks to Mr. Jiayin Zhou for his helpful idea and comments. Lastly, I would like to thank my husband and my parents for their endless love and support.

Sima Taheri

July 2007

Contents

Summary

Three-dimensional segmentation is reliable approach to achieve an accurate estimate of the tumor volume. This estimate is useful for several applications such as assessing tumor growth, assessing treatment responses, planning radiation therapy, and constructing tumor growth models. Among all possible methods for this purpose, the level set is a powerful tool which implicitly extracts the tumor surface. The major challenge of the level set algorithms is to set the equation parameters, especially the speed function. In this thesis, we propose two level-set based approaches for 3D tumor segmentation. The first approach introduces a threshold-based scheme that uses level sets for tumor segmentation (TLS). In this scheme, the level set speed function is designed using a global threshold. This threshold is defined based on the idea of confidence interval and is iteratively up-

dated throughout the evolution process. Two threshold-updating schemes, search-based and adaptive, are provided in this approach that require different degrees of user involvement. In the second approach, one-class SVM (support vector machine) algorithm is integrated into the level set method. Knowing the advantage of one-class SVM in handling the nonlinear distributions without additional prior knowledge, we design an appropriate speed function for the level set. In order to train the SVM, the samples inside the zero level set are used and the training is iteratively refined as the level set grows. Both schemes do not require explicit knowledge about the tumor and non-tumor density functions and can be implemented in an automatic or semi-automatic form depending on the complexity of the tumor shape. Moreover, these schemes can segment both homogeneous and non-homogeneous tumors. These approaches are examined on 16 MR images and the experimental results confirm their effectiveness. The segmentation results of these approaches are quantitatively compared with each other and also with the results of an existing region-competition based method. The comparison results indicate the superior performance of TLS.

List of Tables

List of Figures

Chapter 1

Introduction

1.1 Motivation

Magnetic resonance imaging (MRI) of the brain is often used in tumor diagnosis, monitoring tumor progression, planning treatments, and monitoring responses to treatment. For these purposes, having an accurate estimation of tumor size is very useful. Although maximum tumor diameter is widely used as an indication of tumor size, it may not reflect a proper assessment of this tumor attribute because of the 3D nature and irregular shape of the tumor [1, 2]. Tumor volume, on the other hand, may be an appropriate representation of tumor size. Therefore developing the objective, accurate, and reliable methods for measuring tumor volume are very important.

One way to obtain an estimate of tumor volume is via segmentation. Such

schemes implicitly acquire tumor volume by extracting the tumor surface. Although numerous methods have been proposed to detect the tumor surface from magnetic resonance (MR) images, we refer to some of them in Chapter 2, there is no standard solution for this purpose so far. The increasing need for the tumor boundary/surface detection approaches and the challenge of method development motivate us to continue the research work in this area. We try to achieve a practical, reliable, and validate method for 3D tumor segmentation in the MR images.

1.2 Magnetic resonance imaging

MRI is a method of looking inside the body without using surgery or x-rays. It uses magnetism and radio waves to produce clear pictures of the human anatomy. MRI is based on a physics phenomenon discovered in the 1930s, called nuclear magnetic resonance (NMR), in which magnetic fields and radio waves cause atoms to give off tiny radio signals. This imaging medium has been of particular relevance for producing images of the brain, due to the ability of MRI to record signals that can distinguish between different soft tissues such as gray matter and white matter [3]. In imaging the brain, two of the most commonly used MRI visualizations are T1-weighted and T2-weighted images. These modalities refer to the dominant signal measured to produce the contrast observed in the image [3]. Since areas with high fat content have a short T1 time relative to water, T1-weighted images

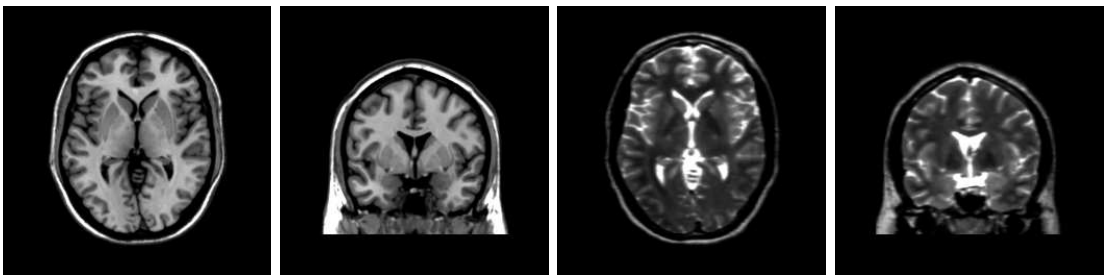

Figure 1.1: T1- and T2-weighted MR images. Left to right: T1 axial and coronal images (light regions visualize locations of fat), T2 axial and coronal images (light regions visualize locations of water).

visualize the locations of fat. In contrast, since areas with high water content have a short T2 time relative to areas of high fat content, T2-weighted images visualize the locations of water. Figure 1.1 shows two examples of T1- and T2-weighted MR images. A summary of T1 and T2 effects on the MR images is given in Table 1.1.

Table 1.1: A summary of T1 and T2 effects on the MR images. TR= repetition time; TE=echo time [3].

Pulse Sequence (TR/TE)	**Effect** (Signal Intensity)	**Tissues**
T1-weighted (short/short)	Short T1 relaxation (bright)	Fat, Proteinaceous Fluid, Paramagnetic Substances (Gadolinium)
	Long T1 relaxation (dark)	Neoplasm, Edema, CSF, Pure Fluid, Inflammation
T2-weighted (Long/long)	Short T2 relaxation (dark)	Iron containing substances (blood breakdown products)
	long T2 relaxation (bright)	Neoplasm, Edema, CSF, Pure Fluid, Inflammation

Both T1 and T2 images are acquired for most medical examinations; However, they do not always adequately show the anatomy or pathology. In visualizing brain tumors, a second T1-weighted image is often acquired after the injection of a contrast agent. These contrast agent compounds usually contain an element like gadolinium whose composition causes a decrease in the T1 time of nearby tissue. This results in bright regions observed at image locations that contain leaky blood cells. The presence of this type of enhancing area can indicate the presence of a tumor [3].

Figure 1.2 illustrates a T1 image before and after the injection of a contrast agent. While the presence of this enhancement can be a strong indicator of tumor location, there exist a large variety of types of brain tumors, and their appearance in MR images can vary considerably. Although some may be fully enhancing or may have an enhancing boundary, many types of tumors display only partial enhancement or no enhancement at all.

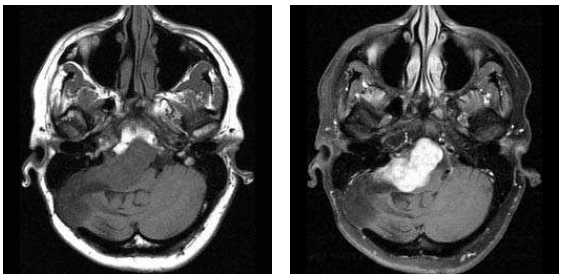

Figure 1.2: Effects of contrast agent on T1 image. Left: T1 image before the injection of a contrast agent. Right: T1 image after the injection of a contrast agent.

1.3 Problem definition

The problem addressed in this thesis is the three-dimensional (3D) segmentation of the brain tumors in multi-spectral MR images. This is a difficult task that involves various disciplines covering pathology, MRI physics, radiologist's perception, and image analysis based on intensity and shape. Since the first step in solving a problem is to have a good definition of it, this section outlines our problem definition.

In this problem, the inputs are the multichannel 3D MR images of the head that show the tumor region. Each 3D MR image is a series of slices taken from the same individual in the same session. Our dataset contains the MR images of 16 patients. Figure 1.3 shows some of these 3D MR images. Since high resolution MR images are required for 3D segmentation and T2-weighted MR images are often difficult to obtain in high resolution due to technical limitations, we use T1 modalities in this work.

The output of this work is the 3D surface of the tumor. There are two kinds of methods to obtain the 3D tumor surface. One is reconstructing the 3D surface from a sequence of 2D contours detected in the parallel cross-sectional images [4]. We call it the pseudo-3D approach. An example of this mechanism is shown in Figure 1.4. The main disadvantages of this group of methods are: (a) a broken boundary in one slice usually leads to poor detected results, (b) a segmentation of a slice along different axes may lead to different results, and (c) the reconstruction

of the surface and its properties from 2D contours may lead to inaccurate results.

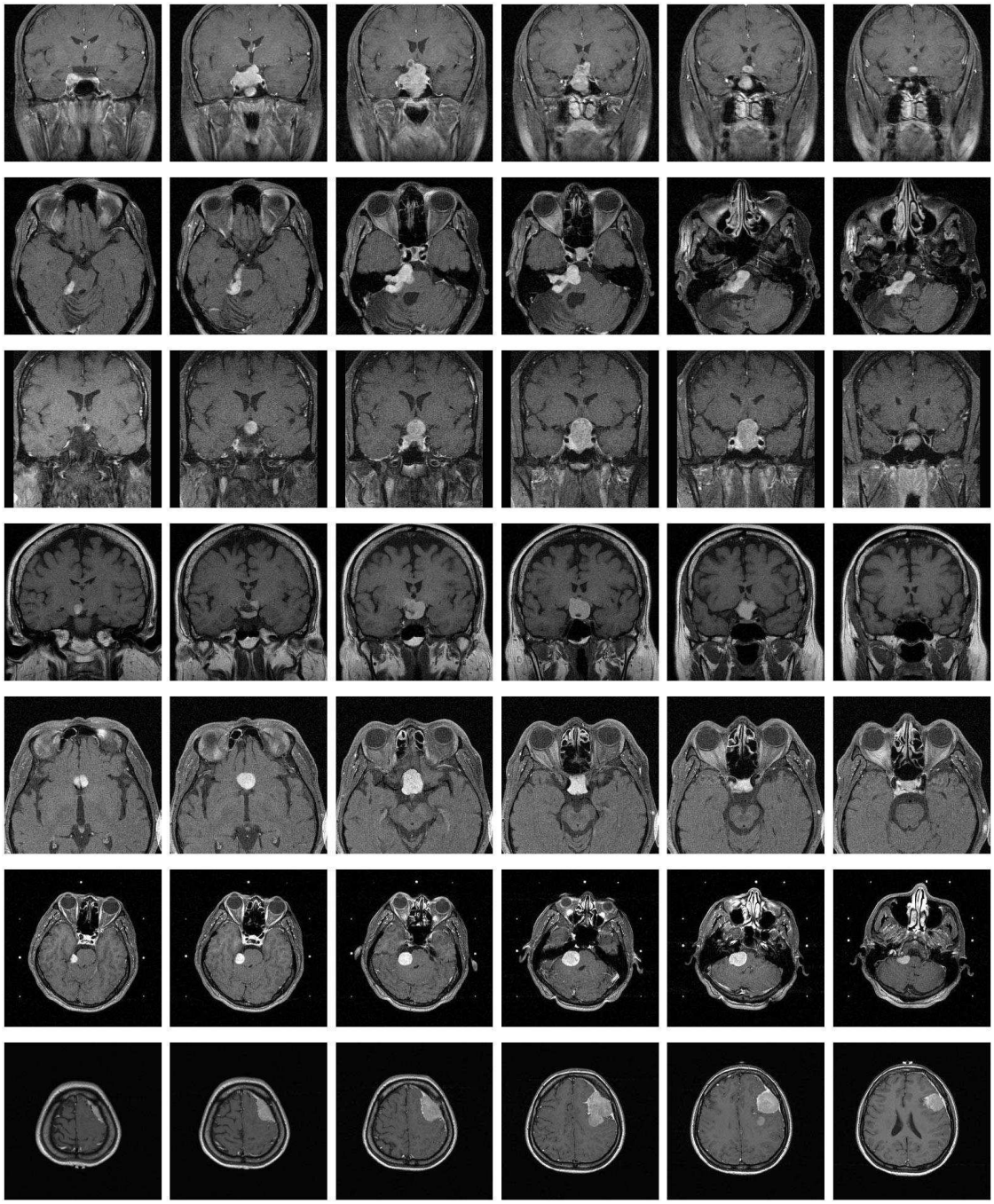

Figure 1.3: Some slices of 3D MR images in the dataset. The indexes of MR images from top to bottom are: 2, 3, 5, 6, 8, 11 , and 13.

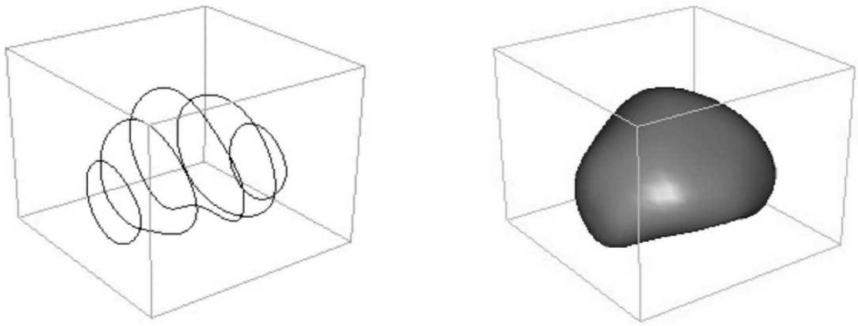

Figure 1.4: Example of pseudo-3D approach [5].

Another method for 3D segmentation, which is believed to be more robust and accurate, is to carry out the computation in 3D space and detect the 3D tumor surface directly. We call it a volume approach. Accordingly, our work is concentrated on the volume approach.

The goal of this thesis is to develop methods for 3D tumor surface extraction from T1-weighted MR images with minimal user involvement. Since the desired output is defined manually by human experts based on the visible abnormality in the image data and this task is limited by the imaging protocol, the goal is not to determine the absolute location of the tumor, but to perform the segmentation like a human expert.

1.4 Overview of methodology

The study of automatic brain tumor segmentation represents an interesting research problem in machine learning and pattern recognition. However, developing highly accurate automatic methods remains a challenging problem. This is because humans must use high-level visual processing and must incorporate specialized domain knowledge to perform this task, which makes developing fully automatic methods extremely challenging.

In this thesis we introduce two algorithms for 3D tumor segmentation using the level set approach in the MR images. Unlike the standard level set methods, the tumor and non-tumor region information is embedded in the level set speed function to automatically extract the 3D tumor surface. The first approach called TLS uses the level set as a deformable model and defines its speed function based on intensity thresholding so that no explicit knowledge about the density functions of the tumor and non-tumor regions are required. The threshold is updated iteratively throughout the level set growing process.

The second method is a SVM-based approach which again uses the level set as a deformable model and defines its speed function on the basis of one-class SVM training and testing process. Therefore, as in TLS approach, no explicit knowledge about the density functions of the tumor and non-tumor regions are required. Moreover, using one-class SVM leads the user interaction to be reduced

to a simple level set initialization and removes the time consuming non-tumor sampling. In order to train the SVM, samples inside the zero level set are used and the training is iteratively refined as the level set grows.

1.5 Thesis contribution

The key contributions of the first approach, presented in Chapter 3, are as follows.

- Using the tumor and non-tumor intensity information to replace the image gradient term in the level set speed function. The key task of level set methods is to provide an appropriate speed function that can drive the evolving front to the desired boundaries. The standard level set methods generally use the image gradient to define this speed. However, they suffer from the weak image gradient information in the MR images. Therefore, we incorporate the intensity information into the level set method and define an image-based factor, F_I to discriminate the tumor and non-tumor pixels and thereby improving the algorithm performance.

- Defining a global threshold that is updated iteratively to form the F_I term in the level set speed function. We use the concepts of confidence interval and confidence level based on the Chebyshev inequality to define a proper threshold for the tumor region. Since the Chebyshev inequality holds without

any assumption regarding the shape of the distribution, density estimation of the tumor and non-tumor regions is unnecessary.

- Proposing two schemes for updating the threshold and converging to the final threshold value. In our approach, the initial threshold is calculated based on the level set initialization and then, it is updated throughout the process of segmentation, iteratively. We propose two threshold-updating schemes, search-based and adaptive. These two schemes require different degrees of user involvement.

- Using an automatic or semi-automatic initialization for the level set depending on the complexity of the tumor shape. A spherical surface is used as the initial zero level set and depending on the convexity or concavity of the tumor shape, different number of initial surface is required. Moreover, by defining the reference slice, a simple scheme for initializing the level set is achieved.

- Defining an appropriate stopping criterion for the level set method. When the zero level set reaches the tumor boundary, variation of the threshold declines, because of the contrast between tumor and non-tumor intensities. We use this idea to define a stopping criterion based on the variance of the threshold values in the final iterations.

The second approach, discussed in Chapter 4, uses one-class SVM to classify the samples. The level set is then grown on this classified data to extract the tumor surface. In this approach, the level set speed function is also defined based on the region information. The level set initialization phase in this method is completely the same as the first one. Our contributions in this approach are as follows.

- Using one-class SVM to define the image-based factor in the level set speed function. Knowing the advantage of one-class SVM in handling the nonlinear distributions without additional prior knowledge, we design an appropriate speed function for the level set. Therefore, as in the first approach, density estimation of the tumor and non-tumor regions is unnecessary.

- Training the SVM iteratively. Since, in most of the cases, tumors have non-uniform intensities, SVM cannot result in good classification using a small training set, and the result depends on the training set. To address this problem, the SVM training is iteratively refined as the level set grows.

- Defining an appropriate stopping criterion for the level set method. At the tumor boundary, the negative speed of the level set for non-tumor samples declines the rate of accepting new samples so that the variations of the zero level set volume becomes negligible per iteration. This idea is used to define an appropriate stopping criterion for this approach.

1.6 Organization of the thesis

The remaining chapters of the thesis is organized as follows.

Chapter 2 surveys a variety of techniques proposed in the literature for the brain tumor segmentation in the MR images and discusses their advantages and disadvantages.

Chapter 3 introduces a threshold-based scheme that uses level sets for 3D tumor segmentation (TLS). In this chapter, a preliminary knowledge about the level set and its mathematical background is provided. After that, different parts of the TLS approach are discussed in details and the simulation results are shown.

Chapter 4 introduces a SVM-based algorithm that benefits the level set for 3D tumor segmentation in the MR images. Details of two-class and one-class SVM are covered in this chapter. A segmentation algorithm based on one-class SVM is provided and different parts of it are described. The simulation results are also provided.

Chapter 5 presents a validity evaluation of the proposed approaches. The results of the proposed schemes are compared with each other and also with the results of an existing method for tumor segmentation. The outcomes of these evaluations are presented in this chapter.

Chapter 6 concludes the thesis and provides the possible future work for continuing research.

Chapter 2

Brain Tumor Segmentation Approaches

There is a huge array of scientific literature focusing on the task of image segmentation. Medical image segmentation has also received significant attention, due to the many practical applications of segmentation results. An impressively large amount of research effort has even focused on specific areas of the body or specific modalities, such as the segmentation of brain in the MR images. This chapter provides an overview of the approaches used to solve the problem of the brain tumor segmentation. Therefore, the focus of this section may seem limited in scope; however, there has been a large amount of research effort directed towards this problem and some of these approaches that are discussed here represent examples of state of the art methods in this area of medical image segmentation.

Tumor segmentation approaches are categorized into several groups according to the segmentation mechanism they applied. This section presents a review on

common methods that have appeared in recent literature for tumor segmentation. The remainder of this chapter is divided into four sections, namely, supervised segmentation, unsupervised segmentation, segmentation using spatial prior probabilities, and level-set segmentation. The difference between supervised and unsupervised approaches is that the supervised methods make use of the training data that has been manually labeled, while unsupervised methods do not.

The existing approaches perform tumor segmentation in either 2D or 3D space. Two-dimensional approaches refer to those methods that extract the boundary of the tumor in 2D tumor slices while the other algorithms perform directly on the 3D images of the tumor. In the last section we discuss the 3D segmentation approaches that use level set method to extract the 3D tumor surface. Although these methods may be included in the other sections, they are grouped in a separate section since our work is concentrated on the level set method.

2.1 Supervised segmentation

Supervised approaches for image segmentation differ from unsupervised methods in the use of labeled training data. A popular way to perform image segmentation using a supervised approach is the classification problem formulation that assigns a class, from a finite set of classes, to an entity based on a set of features. Supervised classification involves both a training phase and a testing phase. In the training

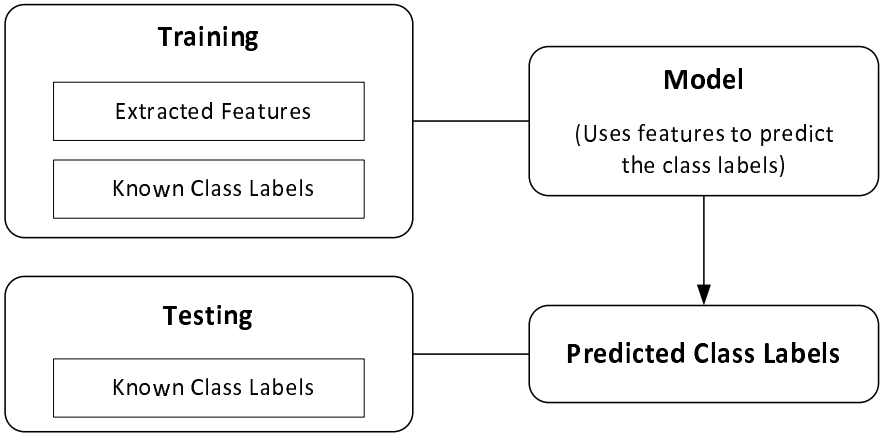

Figure 2.1: Supervised learning framework.

phase, the labeled data is used to automatically learn a model for segmentation. In the testing phase, this model is used to assigned labels to the unlabeled data (Fig. 2.1). A major advantage of using a supervised formulation is that supervised methods can perform different tasks simply by changing the training set.

The brain tumor segmentation task can be formulated as a supervised classification problem by using the tumor and non-tumor labels as two classes and the intensities in the different MR images as the features. In this formulation, the training phase consists of learning a model to discriminate between tumor and non-tumor pixels using the MR image intensities and the testing phase consists of using this model to classify unlabeled pixels into one of the two classes based on their intensities.

One of the first studies on the supervised classification approach for brain tumor segmentation in MR images has been done by Clarke [6]. He compared a

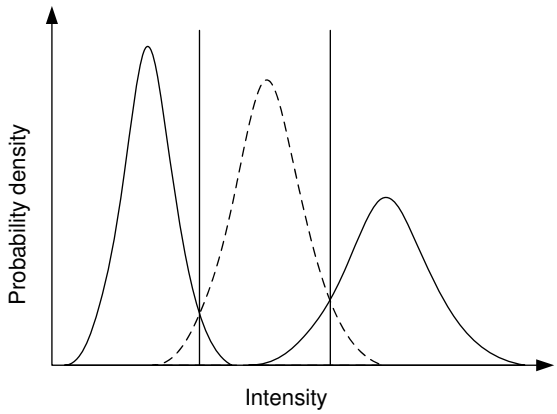

Figure 2.2: A simple maximum likelihood classification model (three classes). Classifications are made by assigning pixels to the class with the highest probability density based on its intensity.

maximum likelihood (ML) classifier with an artificial neural network (ANN) and found that the ANN performed better than the ML approach. The training phase in ML classifiers consists of optimizing the parameters of a parametric model such as a univariate or multivariate Gaussian, and assigning the pixels to the class that they are statistically most likely to belong to, based on these models (Fig. 2.2). In contrast, ANN approaches feed the features through a series of nodes, where mathematical operations are applied to the input values at each node and a classification is made at the final output nodes (Fig. 2.3).

The training phase for these models consists of determining the values of the parameters for the mathematical operations such that the error of predictions, made by the output nodes, is minimized. ANN approaches are non-parametric techniques since no parametric distribution (such as a Gaussian distribution) is as-

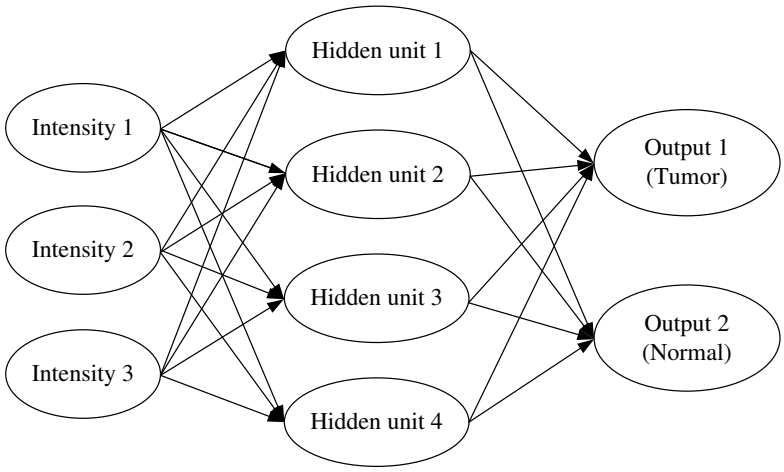

Figure 2.3: Artificial neural network architecture. Pixels are assigned to the class whose output node has the highest value.

sumed for the data. Moreover, they allow the modeling of non-linear dependencies in the features via hidden layers. Although training of ANN models is more complex than simpler ML models, the ability to model non-trivial distributions offers clear practical advantages. This is noteworthy in the case of tumor segmentation since assuming a simple Gaussian distribution for the data may not be appropriate.

Vinitski *et al.* [7] presented a supervised method that addresses several issues of the most automatic systems for tumor segmentation. Several preprocessing steps are used in this method to improve the results:

- Co-registration of the different modalities to improve their alignment
- Using an anisotropic diffusion filter, which is a method for edge-preserving nonlinear smoothing, to reduce the effects of local noise on the classification.

- Using an intensity inhomogeneity correction algorithm to reduce the errors associated with the intensity inhomogeneity present in the images.

This method uses patient-specific training and classifies the T1-, T2-, and ρ-weighted images (an additional MR modality that is often acquired simultaneously with T2 images) into 10 tissue classes. The k-nearest neighbors (kNN) classifier is used that assigns labels to pixels based on the most frequent label among the k nearest training points. The kNN algorithm is a simple and effective method for multi-class classification, that is able to model non-linear distributions. Disadvantages of the kNN algorithm include the dependency on the parameter k, large storage requirements (the model consists of all training points), sensitivity to noise in the training data, and the undesirable behavior that occurs when a class is under-represented in the training data [8].

One of the recent approach in automatic tumor segmentation has been presented by Zhang *et al.* [9]. This approach uses support vector machine (SVM), which is currently a popular method for binary classification. SVM is covered in detail in Chapter 4, since one of the approaches presented in this work, uses this classification method. Zhang proposed a simple system for the segmentation of nasopharyngeal carcinomas (a highly localized type of tumor). In this approach, the SVM is used for binary classification into either the tumor or non-tumor class based on the T1 pre- and post-contrast MR images.

This system uses patient-specific training and compares two different types of the SVM, the standard two-class method and the more recent one-class method. The advantage of using a one-class SVM is a reduction in the manual time needed to perform patient specific training, since only training examples from the tumor class is needed. However, the disadvantage of this method is that the segmentation result is very dependent on the training set such that a small training set may not give a good segmentation result.

Garcia and Moreno [10] proposed another recent approach for automatic brain tumor segmentation using SVM. This work also uses patient specific training. In this work, the intensities of a neighborhood of the pixels are used for classifications. A two-class SVM is used for the initial pixel classification, followed by a one-class SVM that constructs a 3D tumor model.

The supervised methods of brain tumor segmentation are highly effective and versatile, but they often suffer from the disadvantage of requiring patient-specific training. However, there are some exceptions that are able to perform inter-patient classification, but they mostly focus on relatively simplified tasks and require a large amount of training data.

2.2 Unsupervised segmentation

Gibbs *et al.* [11] presented an unsupervised approach for the segmentation of tumor in T1 post-contrast MR images. In this system, first an intensity threshold is applied to a manually selected region of interest, then a region growing algorithm is used to expand the thresholded regions up to the edges defined by a Sobel edge detection filter. Figure 2.4 demonstrates intensity thresholding and Sobel edge detection results.

As can be seen in this figure, some amount of false positives are associated with normal structures in both thresholded images, especially in the third image (from left to right), and false negatives are associated with regions that do not have sufficiently high intensity, especially in the second image. The region growing result is refined through iterations of dilation (causing the defined tumor region to grow), and erosion (causing the defined tumor region to shrink). These two

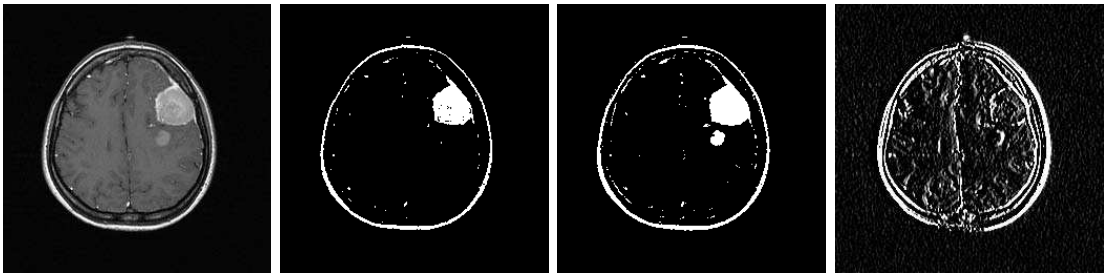

Figure 2.4: Examples of low-level image processing in segmentation of enhancing tumor. Left to right: T1 post-contrast image, image after intensity thresholding, image after intensity thresholding with lower value of threshold, and edge probabilities resulting from a Sobel filter.

operations change the labels assigned to individual pixels by examining the labels of neighboring pixels, and are commonly referred to as morphological operations. A similar approach was proposed in [12] for the segmentation of the enhanced tumor pixels.

These approaches present a method for segmenting image objects that are different in intensity compared to their surroundings. The disadvantages of these approaches are as follows:

- These methods do not effectively take into account the presence of pixels with high intensity representing normal structures in T1 post-contrast images.
- The assumption that the entire boundary has a large intensity difference with its surrounding tissues is not always the case.

Clark *et al.* [13] presented an unsupervised tumor segmentation approach which is one of the most validated system to date. Their work focuses on the segmentation of post-contrast T1 , T2, and ρ-weighted images. The two main components of this system are fuzzy C-means (FCM) clustering and a linear sequence of human-engineered knowledge-based rules and operations. In the clustering part of the algorithm, pixels are divided into groups based on their intensities, while in the knowledge-based part, a set of rules and low-level image processing operations process the results of the clustering algorithm in order to achieve a final segmentation. These rules enable the algorithm to identify the clusters that do not have

tumor properties. Therefore, the clustering process starts from the entire image and proceeds to the very specific areas (Fig. 2.5).

Examples of these rules are: (a) cerebrospinal fluid (CSF) is the cluster within the brain that has the lowest T1 value, (b) pathological pixels are assigned to the 3 highest intensity ρ-weighted clusters, and (c) clusters with tumor pixels are closer to the highest T1 cluster than the lowest. Moreover, the image processing rules include morphological operations such as erosion and closing, in addition to cluster evaluation techniques such as cluster density thresholding. Note that these rules are not learned automatically from the data, but rather are manually engineered by the designer.

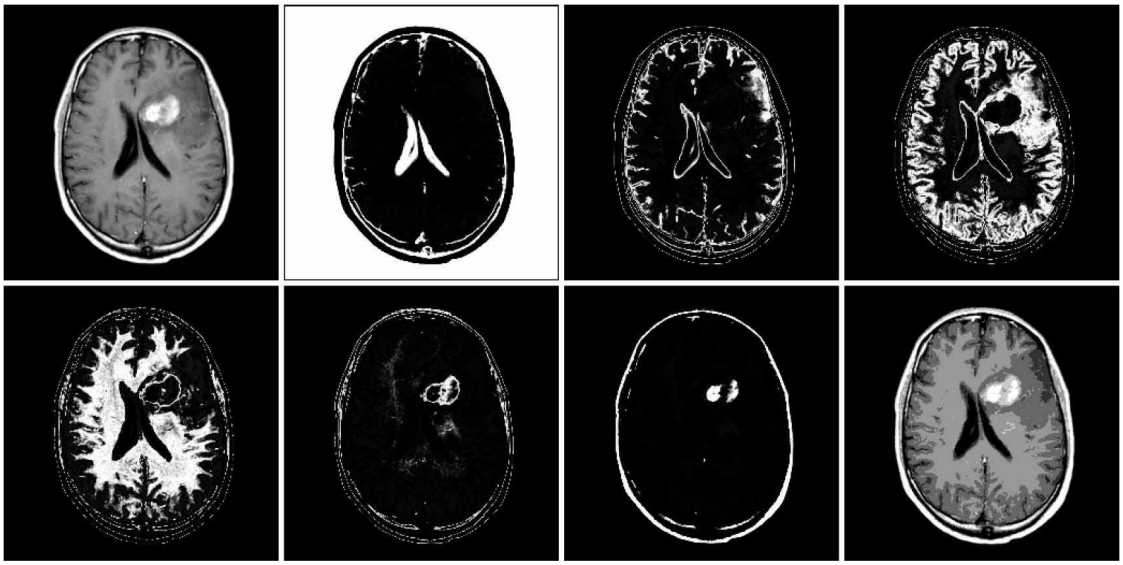

Figure 2.5: Example of fuzzy C-means clustering into 6 clusters. First row, left to right: post contrast T1 image and first three clusters. Second row, left to right: last three clusters and image visualizing all 6 clusters [14].

An obvious advantage of this system is the rules that account for normal structures with high intensity. However, there are some disadvantages associated with such knowledge-based approach and the most important one is that it requires considerable manual engineering. This is primarily due to the difficulty of translating complex anatomic knowledge and visual analysis into the low-level operations and rules. Even for the simplest definition of tumor segmentation, the final system requires a large amount of rules and manual data analysis. Therefore, such systems cannot be used for the cases where tumor tissue is similar to the normal tissue, does not have a clearly defined boundary, or is non-homogeneous.

This type of approach has been employed in various works. More recent systems based on the FCM and knowledge-based rules include [15], which focuses on the segmentation of non-enhancing tumors, and [16], that incorporates intensity standardization as a preprocessing step and utilizes a modified FCM algorithm with dependencies between neighboring pixels.

Another unsupervised approach has been presented by Capelle *et al.* [17]. Their method has advantages over similar methods due to the use of an automatic brain masking preprocessing operation. This operation removes those pixels from the analysis that are not part of the brain area. Another advantage of this method is the use of a Markov random field model that removes the need for morphological operations. This work assumes that the tissue classes (gray matter, white matter, CSF, tumor, and edema) could be modeled by a Gaussian mixture model.

Moreover, it trains the Markov random field using the iterated condition modes (ICM) algorithm. More recently, Capello *et al.* presented another approach of this nature,[18], that also uses brain masking and a Gaussian mixture model that is learned using an expectation maximization (EM) approach, but it uses an evidence theory formulation rather than a Markov random field to take the neighboring pixel dependencies into account.

Unsupervised segmentation approaches are preferred to supervised methods since they do not need any training data and thus need less user interaction. However, the application of such algorithms is limited and most of them have focused solely on the segmentation of enhancing tumor areas. This is because the visualization information and anatomic knowledge are difficult to be translated into the operations that yield the desired results.

2.3 Segmentation by spatial prior probabilities

Expectation maximization approach is a popular framework for segmentation of the head MR images into the three normal brain classes (grey matter, white matter, and CSF) since it is robust to both intensity inhomogeneity and intensity non-standardization. The spatial prior probabilities for these three classes are provided with statistical parametric mapping (SPM), which is derived from the work of Evans *et al.* [19, 20]. These prior probabilities represent the empirical likeli-

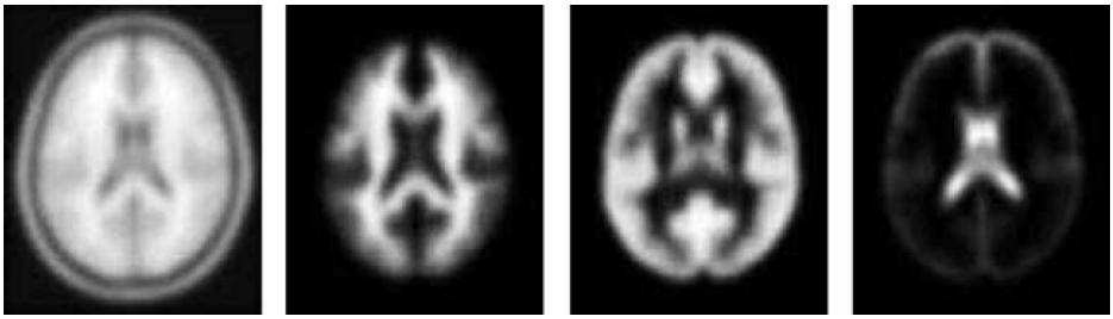

Figure 2.6: SPM priors [21]. Left to right: T1 registration template, gray matter spatial prior probability, white matter spatial prior probability, and CSF spatial prior probability.

hood that a pixel in an image, registered into the standard coordinate system of the template, belongs to each of the three classes. Figure 2.6 shows these prior probability images.

Several factors complicate the application of EM approach to brain tumors segmentation. The first factor is that there is no prior knowledge available for the tumor class. Therefore, the tissue class parameters cannot be initialized using the prior probabilities. Tumor heterogeneity is a second factor that complicates the direct application of this algorithm, since heterogeneous tumors are not modeled effectively by Gaussian distributions. The final complication of applying this algorithm to tumor segmentation is that tumor and non-tumor tissues may have similar intensities and it is difficult for this approach to discriminate between different areas with similar or the same intensities.

Moon *et al.* [22] proposed the first approach for tumor segmentation based on

the EM method with spatial prior probabilities. In their work, a prior probability for enhancing tumor pixels is approximated from the contrast agent difference image while edema is assumed to be collocated with the white matter. In the preprocessing phase, the modalities are aligned and the template registration is done using a linear affine transformation. Then, the EM segmentation method is applied to T1 pre-contrast and T2 images for the segmentation of tumors with an enhancing boundary and edema. Unfortunately, this approach is only applicable to the enhanced tumors, and it is not obvious how to obtain a meaningful prior probability approximation for more difficult cases.

Gering *et al.* [23] outlined another approach using a variation of EM. This approach also detects tumors as intensity outliers from normal tissues. In this work, the EM results are refined using a Markov random field. It presents a method to discriminate partial volume pixels from tumor pixels via creating an adaptive spatial prior probability for pixels that are at the boundaries of the normal structures. These additions to the EM algorithm are combined into a structured contextual-dependency network for the segmentation of brain tumors in T1 images. The multi-level Markov random field in particular addresses a major weakness of the EM methods since it allows the identification of tumor structures that have normal intensities. Unfortunately, this method is only applicable to tumors that are homogeneous enough to be segmented into a single normal tissue class, and therefore is not generally applicable to non-homogeneous tumors.

2.4 Level-set segmentation

Level set method [24] is a type of finite element approach used for the modeling of active curves or surfaces. This method has recently been applied within the field of machine vision for segmentation problems, especially for 3D segmentation. Unlike the traditional deformable models, the level set method does not depend on the parameterization of the fronts, but only on their velocities. This makes it very attractive and flexible in shape modeling and image segmentation.

Level set approach offers several advantages, the important of which are the ability to handle complex geometry and topological changes and their numerical stability. Another attractive advantage of the level set method is that, given an initial zero level set (initial hypersurface), the entire segmentation procedure is fully automatic. Moreover, unlike other methods, the extension of the algorithm to 3D is straightforward and without any additional machinery. Furthermore, the initial hypersurface can be chosen freely, i.e, it is not necessary to be close to the desired boundary (as in the snake algorithms) and thus user interaction is reduced [24]. These advantages motivate us to select this approach as our 3D segmentation tool. In Chapter 3, the level set is discussed in detail.

Leventon *et al.* [25] proposed a novel method of incorporating prior shape information into the level set method for medical image segmentation. In this work a representation for deformable shapes is introduced and a probability distribution

over the variances of a set of training shapes is defined. The segmentation process embeds an initial curve as the zero level set of a higher dimensional surface, and evolves the surface such that the zero level set converges on the boundary of the object to be segmented. At each step of the surface evolution, the maximum a posteriori (MAP) position and shape of the object is estimated based on the prior shape information and the image information. The surface is evolved, globally towards the MAP estimate, and locally based on image gradients and curvature.

An adaptive multi-grid level set method for 3D medical image processing and segmentation has been presented by Droske *et al.* [26]. Using a flexible and interactive modulation of the level set speed function, this method is able to deal with non-sharp boundaries. The main difficulties of the level-set segmentation methods is that their formulation usually entails several free parameters that must be tuned for specific applications. Lefohn *et al.* [27] presented a level set surface model that is computed at interactive rates on commodity graphics cards (GPUs). In their method, the interactive rates for solving the level set partial differential equation give the user immediate feedback on the parameter settings, and thus users can tune the separate parameters and control the shape of the model in real time.

A powerful software package for interactive segmentation of 3D images using level sets has been designed by Ho *et al.* [28]. Several variants of level set methods are incorporated in this software, including both gradient-magnitude based level set as well as region-competition level set. A complete segmentation pipeline, including

image preprocessing, bubble initialization and parameter control, is provided in an intuitive user interface. This tool is already in daily use by clinicians and offers a good improvement in speed over traditional manual segmentation.

Ho *et al.* [29] also presented a recent fully unsupervised approach for 3D tumor segmentation using the level set method. Although their approach focuses on segmenting tumors with an enhancing border, it is not subject to many disadvantages of the other approaches presented in the previous sections. This system uses both the T1 pre- and post-contrast images as input, and the first step in this system is the spatial alignment of these two volumes. After that, the difference between these two images is computed as a new image (Fig. 2.7). The histogram of the difference image is fitted by parametric distributions (a Gaussian mixture model) for both the enhanced parts and the noisy background. Using this fitted distribution, the difference image is mapped to the tumor posterior probability that is used in the level set speed function.

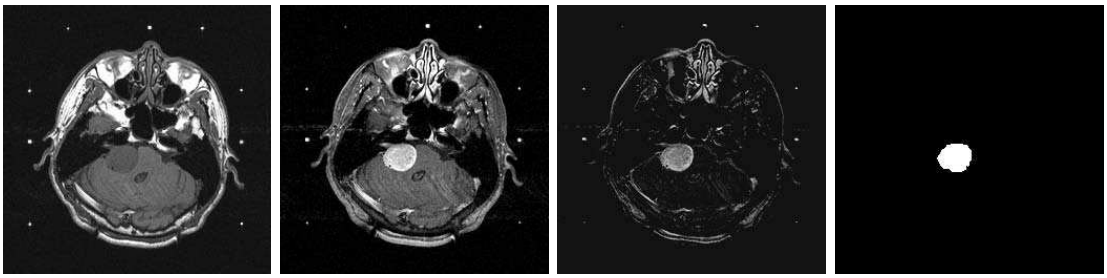

Figure 2.7: Example of Ho *et al.* method. Left to right: original T1 image, aligned T1 post-contrast image, pixel-wise difference image, and segmentation result.

The Ho *et al.* method has clear advantages over the methods discussed earlier. The use of a mixture model allows the technique to adaptively find the enhanced area, and is thus more robust to difference in intensity between images due to intensity non-standardization. Another advantage of this system is in the case of non-homogeneous tumors, non-enhanced areas surrounded by enhanced areas are included in the segmentation through the use of the level set.

The use of the difference information, rather than the post-contrast image directly, is also advantageous, since it allows false positives associated with the many structures, that have high intensities in T1 images, to be removed. Although this has the potential to remove a significant amount of false positives, there may still be systematic false positives associated with this method, since it does not account for normal structures that are also affected by the contrast agent. Another disadvantage of this system is the large number of parameters that must be set for the level set method to converge to an appropriate solution.

Prastawa *et al.* [30] presented a 3D segmentation approach based on EM methods. This approach uses the level set to extract the 3D tumor surface. The speed of the level set is designed based on the non-parametric estimation (using kernel expansion or Parzen windowing) of tumor and non-tumor distributions. This method does not require contrast enhanced images and the only required input for the segmentation procedure is the T2 MR image. The segmentation framework is composed of three stages. First, the abnormal regions are detected using

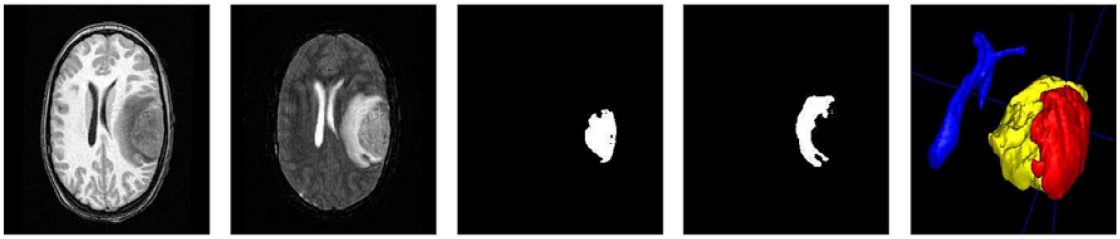

Figure 2.8: Segmentation result by Prastawa method. Left to right: T1 image, T2 image, Tumor, Edema, and 3D view [30].

a registered brain atlas as a model for healthy brains. Then, they make use of the robust estimates of the location and dispersion of the normal brain tissue intensity clusters to determine the intensity properties of the different tissue types. In the second stage, they determine, from the T2 image intensities, whether edema appears together with tumor in the abnormal regions. Finally, geometric and spatial constraints is applied to the detected tumor and edema regions. Figure 2.8 shows an example of segmentation results using this method.

2.5 Conclusion

This section surveyed a variety of techniques proposed in the literature for the brain tumor segmentation. Supervised segmentation methods take advantage of labeled training data and are popular. However, such methods require extensive user involvement and the results are dependent on the training set. On the other hand, although unsupervised segmentation methods avoid the human variability

associated with manual training data, their applications are limited. Moreover, finding the prior information in the EM approaches complicate their applications.

In our opinion, the current state of the art methods for brain tumor segmentation are the level set based approaches that use region information to design the level set speed function [29, 30] along with the SVM-based methods due to the estimation of non-linear distributions without additional prior knowledge [9]. In this work, we extend these approaches by presenting two schemes that use the level set approach for 3D tumor segmentation. In the first scheme, a level set based method is designed using prior information and intensity-based information while in the second scheme, SVM is integrated into the level set segmentation.

Chapter 3

Threshold-based 3D Tumor Segmentation Using Level Set Method

In the previous chapter, we discussed some of the approaches presented in the literature for the brain tumor segmentation. In general, the proposed methods vary widely depending on the specific application and imaging modality. The same algorithm which gives excellent results for one application might not even work for another. General imaging artifacts like noise, partial volume effects, intensity inhomogeneity and inter-slice intensity variations can significantly affect the outcome of a segmentation algorithm. These variabilities make volume segmentation in medical images a very challenging problem.

In general, a volume segmentation approach consists of more than one segmentation algorithm applied one after the other. Excellent reviews of recent volume

segmentation techniques in medical images can be found in [31, 32]. In this thesis, we select the level set method [24] as the basic algorithm to develop our new approaches for 3D tumor segmentation. In this chapter, we first present the motivation for our proposed approach in brain tumor segmentation, and then describe the different elements of the framework. We begin by briefly reviewing some of the level set based segmentation methods and discussing their limitations. This leads naturally into the motivation for developing our approach. The following sections present the individual components in the segmentation framework.

Active surfaces can be used for 3D segmentation implicitly in the form of the level set or explicitly as a snake function [33]. Among these two approaches, the level set method is preferred and we choose it as the surface detection mechanism in our proposed approach. The reason is because the implicit surface representation in level set approach offers several advantages over snakes. These advantages were discussed in Sec. 2.4. However, there are difficulties in using level sets that make them less desirable in some circumstances. One problem is that the level set formulation entails the tuning of several parameters. The difficulty in adjusting such parameters for specific applications has led to several approaches.

In some methods discussed in Chapter 2, the interactive rates for solving the level set partial differential equation give the user immediate feedback on the parameter settings; the user can therefore tune the parameters and control the shape of the level set in real time [26, 27, 28]. The disadvantage of these methods is that

they increase user interaction and provide good segmentation results only if the user is sufficiently familiar with the level set formulation and the object of interest. Another method, proposed by Leventon *et al.* [25], provides a more generic and automated segmentation of tumor through the combination of level set evolution with statistical shape constraints. In this method, *a priori* shape information is incorporated into a geodesic active contour so that the model parameters are estimated, and the curve then evolves based on that estimation. The problem of this approach is that it may be difficult to obtain statistical prior knowledge in many cases, especially for tumor segmentation.

One of the main parameters in the level set equation is the speed function, whose design is perhaps the most important step in the level set approach. Ho *et al.* [29] proposed region competition in the evolution of the level set, in which the difference between pre- and post-contrast enhanced MR images is used to adjust the speed function. In their method, the histogram of the difference image is fitted by parametric distributions for both the enhanced parts and the noisy background. Using this fitted distribution, the difference image is mapped to the tumor posterior probability for use in the speed function. This idea can be extended based on non-parametric density estimation by kernel expansion or Parzen windowing [30].

The main drawback of such algorithms is their dependency on the accurate estimation of tumor and non-tumor probability density functions. On one hand, the parametric estimation of density functions may not provide sufficient accuracy

because tumors do not generally have uniform intensities. On the other hand, non-parametric density estimation methods such as Parzen windowing require sufficient training samples for both regions. The additional complexity of estimation due to such algorithms motivates us to use density-independent schemes.

Many level set algorithms may be distinguished on the basis of their speed functions. Some approaches, for example, require user interaction while others rely on prior estimation of the tumor density function. In this chapter, we propose a level set method for 3D brain tumor segmentation which employs a speed function that does not require density function estimation and is obtained by minimal user interaction. The basic idea is to use a global threshold to form the speed function.

The initial threshold is calculated using the level set initialization and is then iteratively updated throughout the process of segmentation. Upon reaching the tumor boundary, the variation of the threshold declines because of the contrast between tumor and non-tumor intensities, and the process stops. This algorithm can be implemented in an automatic or semi-automatic form depending on the complexity of the tumor shape. A further advantage is that it can be applied to either pre- or post-contrast T1 MR images and does not require both these images at the same time.

The challenge of our scheme lies in the trade-off between the rate of convergence and the accuracy of segmentation. A high convergence rate is achieved when the

variation of threshold with respect to the iteration number is large. This, however, may lead to low accuracy in segmentation or even destabilization of the algorithm. On the other hand, a small variation of the threshold can guarantee convergence, although at a reduced rate. In this chapter, we study this trade-off and propose an appropriate threshold calculation algorithm. The remaining sections of this chapter outline the components of our framework which are as follows:

- Level set method
- Level set speed function design
- Level set initialization
- Stopping criterion
- TLS analysis
- Segmentation results

3.1 Level set preliminary knowledge

Suppose we are given an interface separating one region from another, and a speed F that tells us how to move each point of the interface. In the Fig. 3.1, a black curve separates a dark gray inside from a light gray outside, and at each point

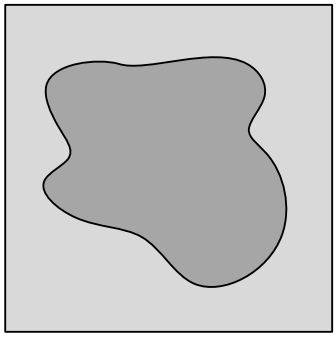

Figure 3.1: An interface separating the image apart.

of the black curve the speed F is given. This speed can depend on a variety of physical effects.

- Imagine that the dark gray is ice and the light gray is water. Then the boundary can shrink as the ice melts, or grow as the ice freezes; the speed then depends on the temperature change between the two regions.

- Imagine that the dark gray is honey and the light gray is tea. Then the boundary moves as the heavy fluid falls into to the light one, and the speed depends on gravity, the ratio of the fluid densities, and the surface tension between the two regions.

Most numerical techniques, such as snakes rely on markers which try to track the motion of the boundary by breaking it up into buoys that are connected by pieces of rope. The idea is to move each buoy under the speed F, and rely on the connecting ropes to keep things straight(see Fig. 3.2). The hope is that more

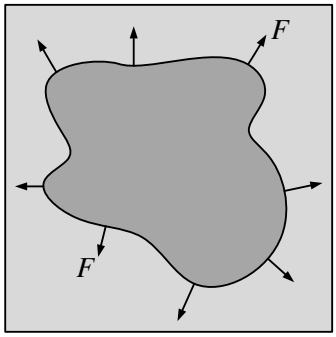

Figure 3.2: Interface moving with the speed F.

buoys will make the answer more accurate.

Unfortunately, things get pretty bad if the buoys try to cross over themselves, or if the shape tries to break into two. In these cases, it is very hard to keep the connecting ropes organized. In three dimensions, following a surface like a breaking ocean wave is particularly difficult.

Rather than follow the interface itself, the level set method instead takes the original curve (Fig. 3.3(a)), and builds it into a surface. That cone-shaped surface, which is shown in blue (Fig. 3.3(b)), has a special property; it intersects the xy plane exactly where the curve sits. The blue surface is called the level-set function, because it accepts any point in the plane as input and feedbacks its height as output. The red front is called the zero level-set, because it is the collection of all points that are at height zero.

Another way to see why this is called a level set surface is to imagine a saw that can cut a slice of the surface and then drop it onto the xy plane. However,

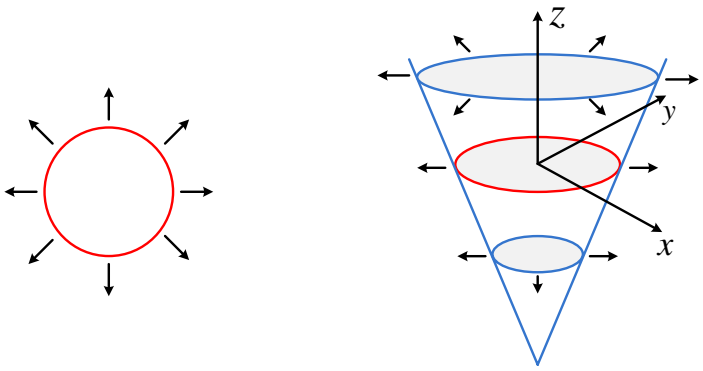

(a) (b)

Figure 3.3: Level-set function and zero level-set, (a) The original front, which lies in xy plane, (b) The level-set function, where the front is intersection of surface and xy plane.

the slice has to be perfectly level.

- If the saw cuts the blue level set surface at height zero above the xy plane, the ring that drops to the xy plane is the original red front.
- If the saw cuts at some other height, a different ring drops down, producing one of the blue curves instead.

3.1.1 Mathematic background

Level set based segmentation involves solving the energy-based active surfaces minimization problem by the computation of minimal distance surfaces in one higher dimension [24, 34]. A parameterized 3D deformable surface,

$$\gamma(r,s) = (x(r,s), y(r,s), z(r,s)), (r,s) \in \Omega : [0,1] \times [0,1] \tag{3.1}$$

is considered as an estimator of tumor surface, where $\mathbf{x} = \{x, y, z\}$ is the coordinate of a surface point. This surface is deformable under the influence of two forces that are internal force and image force. The goal in tumor segmentation is to find the surface γ^* that minimizes the energy function

$$E_T(\gamma) = \int_\Omega E_i(\gamma) + E(\gamma) dr ds \tag{3.2}$$

where the first term

$$E_i(\gamma) = \left[w_{10} \left| \frac{\partial \gamma}{\partial r} \right|^2 + w_{01} \left| \frac{\partial \gamma}{\partial s} \right|^2 + w_{11} \left| \frac{\partial^2 \gamma}{\partial r \partial s} \right|^2 + w_{20} \left| \frac{\partial^2 \gamma}{\partial^2 r} \right|^2 + w_{02} \left| \frac{\partial^2 \gamma}{\partial^2 s} \right|^2 \right] \tag{3.3}$$

is the energy of the internal force that is related to the smoothness of the surface. The second term $E(\gamma)$ is the energy of the image force that is responsible for attracting the surface to the desired object. Depending on what we want the surface to be attracted to, this term can be any related decreasing function of the image gradient or a function of image gray level or other appropriate function of the image.

The surface γ^* that minimizes $E_T(\gamma)$ should satisfy the following Euler-Lagrange equation, which can be obtained using variational calculus method:

$$\nabla E(\gamma(r, s, t)) + \epsilon \kappa_\gamma(r, s, t) = 0 \tag{3.4}$$

Based on this formulation the surface γ is under the control of two forces, the internal force $\epsilon\kappa_\gamma(r,s,t)$ and the image force $\nabla E(\gamma(r,s,t))$.

For solving the Eq. (3.4) we embed γ in a one parametric family $(\gamma(.,t))_{t\geq 0}$ of closed surface, such that as $t \to \infty$ and the surface stabilizes, $\gamma_t(r,s,t) = 0$. As a result, a solution of equation (3.4) is obtained.

$$\frac{\partial\gamma(r,s,t)}{\partial t} = \left[\nabla E(\gamma(r,s,t)) + \epsilon\kappa_\gamma(r,s,t)\right]\mathbf{n}(r,s,t) \tag{3.5}$$

where $\mathbf{n}(.)$ is the unit normal to γ at (r,s) pointing outward and κ_γ is the curvature function of γ.

Eq. (3.5) can be solved numerically by discretizing the domain of γ ($\Omega : [0,1] \times [0,1]$), thus leading to a representation of γ in terms of a finite number of points or nodes. This leads to an explicit representation of γ. A better alternative is to represent the surface γ implicitly by the zero level set of a higher dimensional function $\psi(\mathbf{x},t) : \mathbb{R}^3 \times \mathbb{R}^+ \to \mathbb{R}$ defined by $\psi(\mathbf{x},t) = d$, where d is the signed distance from position $\mathbf{x}$ to $\gamma(t)$. The region inside and outside γ correspond to $\psi < 0$ and $\psi > 0$, respectively.

Since γ obeys an evolution equation, (3.5), and the zero-level set of ψ is assumed to coincide with γ, ψ must evolve according to a certain evolution equation closely related to that of γ [35]. Therefore the evolution equation that ψ has to satisfy so

that its zero level set satisfy the evolution of γ can be expressed as

$$\frac{\partial \psi(\mathbf{x},t)}{\partial t} + \underbrace{[F_A(\mathbf{x},t) - \epsilon\kappa_\psi(\mathbf{x},t)]}_{F} \|\nabla\psi(\mathbf{x},t)\| = 0 \tag{3.6}$$

where F denotes the speed function of the level set. F can be a function of the level set characteristics (e.g. the curvature, normal direction etc.) and the image characteristics (e.g. gray level and gradient etc.). When applied to segmentation problems, the speed term F of the evolving front is usually designed to be dependent on image information, and stop at desired places by having a zero value there. Figure 3.4 shows a diagram of curve propagation to capture the object of interest using the level set method.

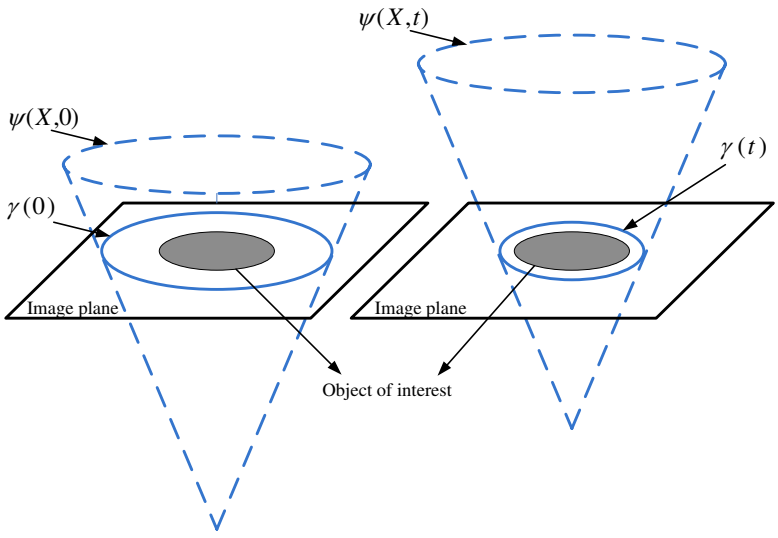

Figure 3.4: Example of 2D curve propagation with the level set method. In this case, the zero level set contracts to capture the oval object on the image plane.

The term κ_ψ is the curvature of the level set given as a function of ψ by

$$\begin{aligned} \kappa_\psi &= \nabla . \frac{\nabla \psi}{\|\nabla \psi\|} \\ &= \frac{\sum_{(i,j,k)\in C}((\psi_{ii}+\psi_{jj})\psi_k^2 - 2\psi_{ij}\psi_i\psi_j)}{2(\psi_x^2+\psi_y^2+\psi_z^2)^{3/2}} \end{aligned} \tag{3.7}$$

κ_ψ is a smoothness parameter which balances the speed of the level set and prevents the level set leaking into many small noisy structures that are not part of the tumor. The strength of this smoothing is controlled via a positive constant factor ϵ which is the entropy condition expressing the importance of regularization. The normal vector of γ can also be easily determined from ψ as follow:

$$\mathbf{n} = \frac{\nabla \psi}{\|\nabla \psi\|} \tag{3.8}$$

The key task in all the level set based methods is to design an appropriate speed function F which can drive the evolving front to the desired object boundary/surface. The original formulation for speed function was given in [24, 36] as

$$F = k_I(F_0 - \epsilon\kappa_\psi) \tag{3.9}$$

where F_0 is a constant term (usually taken as 1) that makes the surface contract or expand and k_I is the data consistency term which ensures the propagating front

will stop in the vicinity of the desired object boundaries. Commonly, k_I is given by

$$k_I(x,y,z) = \frac{1}{1+|\nabla G_\sigma * I(x,y,z)|^p}, p = 1,2 \tag{3.10}$$

where $G_\sigma * I$ denotes the convolution of the image with the Gaussian smoothing filter of characteristic width σ. Clearly, k_I has values close to zero in regions of high image gradient (e.g., possible edges) and close to unity in regions with relatively constant intensity. Compared with the classical energy based snakes model, the term $(F_0 - \epsilon\kappa_\psi)$ acts as the internal force and the external force is given by k_I, which is supposed to prevent the propagating front from penetration into the objects in the image.

Equation 3.10 is an instance of the edge-detector functions. A general edge-detector can be defined by a positive and decreasing function, depending on the gradient of the image, such that $\lim_{z\to\infty} k(z) = 0$. The dependency of these functions on image gradient causes difficulties in the noisy images. As a solution to this problem, Rudin *et al.* proposed an image noise removal algorithm which results in the images with sharp edges [37]. The idea of active contours without edges introduced by Chan *et al.* also tries to tackle this problem [38]. In the following we also propose a level set based algorithm that is not depend on the image gradient.

3.2 Threshold-based segmentation by level set

The level set method described in the previous section can be used for 3D tumor segmentation in MR images. As mentioned before, the key point of the level set method is to design an appropriate speed function, F, which is discussed here.

We assume that the histograms of the tumor and adjacent non-tumor[1] regions slightly overlap. Such an assumption often holds in MR images. Without loss of generality, we assume that the tumor region has mean intensity value greater than that of the background. In such a situation, it is very likely that there exists a threshold which discriminates between tumor and non-tumor voxels. Using the level set, TLS specifies an algorithm to find a proper threshold and a method to update it on an iterative basis. The initial value of the threshold is based on the level set initialization performed by the user inside the tumor region. TLS specifies a speed function on the basis of such a threshold. An important feature of our approach is that explicit knowledge of the density functions of tumor and non-tumor regions is not required.

Figure 3.5 shows two real instances in which appropriate thresholds can be chosen from the shaded intensity ranges, which are where the final (converged) thresholds are very likely to lie. Intuitively, when the densities of the tumor and non-tumor regions are more widely separated, this range is expected to be wider,

[1] area around the tumor boundary and inside the cuboid that encompasses the volume of interest

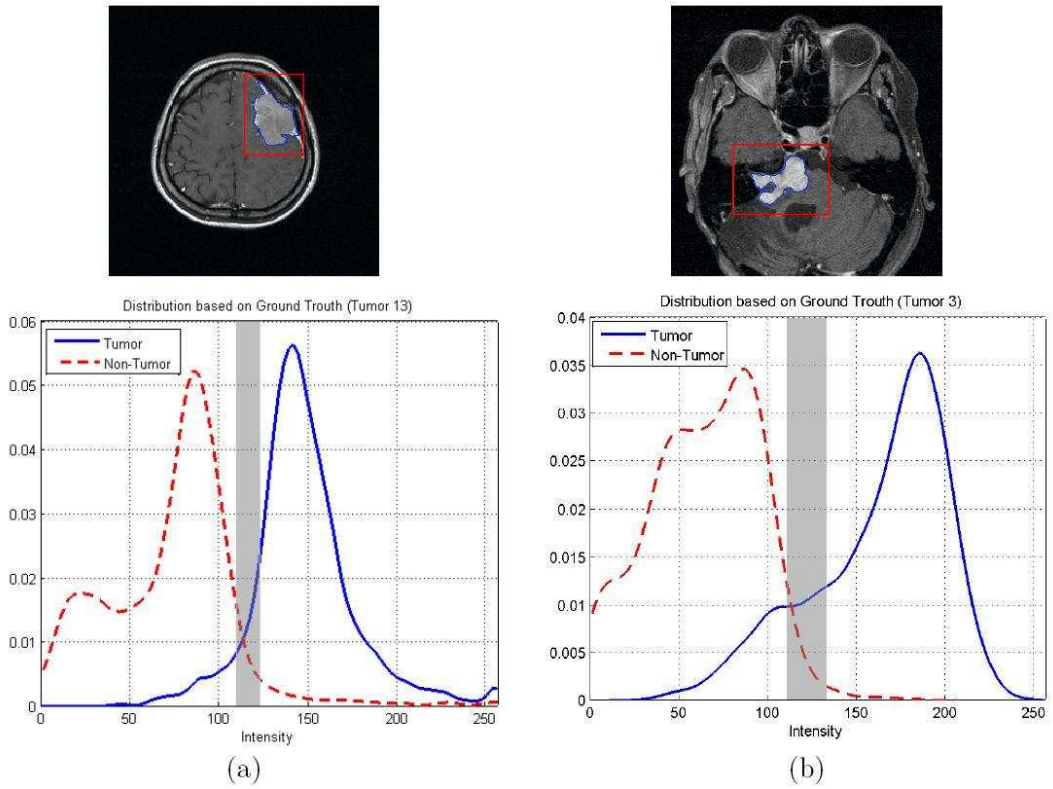

Figure 3.5: Distribution of tumor and non-tumor regions (second row) based on the ground truths in two real MR images (first row).

as can be seen in Fig. 3.5(b). In the figures, the tumor and non-tumor regions are selected based on the ground truths and are inside the volume of interest.

A brief description of the TLS approach is shown in Fig. 3.6. TLS requires an estimate of the threshold to segment the tumor, and this is obtained via the concepts of confidence interval and level. In the following sections, we explain these ideas and their application to threshold estimation. The level set evolution equation is presented and its speed function designed on the basis of our threshold updating approach. Level set initialization and stopping criterion are also discussed.

TLS algorithm

initialize the level set inside the tumor
compute $(\hat{\mu}_0, \hat{\sigma}_0)$ of the selected tumor samples in the reference slice
find the initial threshold, $T_1 = \hat{\mu}_0 - k\hat{\sigma}_0$
while not meet stopping criterion
  compute the speed function, $F^{(i)}$, at each grid point inside the narrow band
  grow the level set
  compute $(\hat{\mu}_i, \hat{\sigma}_i)$ of the tumor samples inside the zero level set
  update the threshold, $T_{i+1} = \hat{\mu}_i - k\hat{\sigma}_i$
  update the narrow band and reinitialize the level set
endwhile

Figure 3.6: TLS algorithm

3.2.1 Confidence interval

The confidence interval (CI) can be defined for any distribution as an interval in which a certain percentage, the confidence level (CL), of observations is located. For a symmetric distribution such as the normal, the CI is within k standard deviations, i.e., $k\sigma$, around the population mean μ. In fact for these distributions (with finite standard deviations), the CL of all observations is located in the interval $\mu - k\sigma$ to $\mu + k\sigma$ (Fig. 3.7(a)).

A general relation between CI and CL can be found based on Chebyshev inequality. It should be noted that Chebyshev inequality holds without any assumption regarding the shape of the distribution as long as the mean and variance exist. For a random variable, ξ, with finite mean and variance, the Chebyshev inequality

$$P(|\xi - \mu| \geq k\sigma) \leq \frac{1}{k^2} \tag{3.11}$$

is valid for any $k > 0$. A variation of this inequality can be expressed as

$$P(|\xi - \mu| < k\sigma) > 1 - \frac{1}{k^2} \tag{3.12}$$

It states that greater than $(1 - \frac{1}{k^2})$ percent of the population falls within k standard deviations from the population mean. For a non-symmetric distribution, the one-tailed version of Chebyshev inequality is appropriate (Fig. 3.7(b)):

$$P(\xi - \mu \geq k\sigma) \leq \frac{1}{1 + k^2} \tag{3.13}$$

Table 3.1 shows the values of Chebyshev inequality and its one-tailed version for some values of k [39].

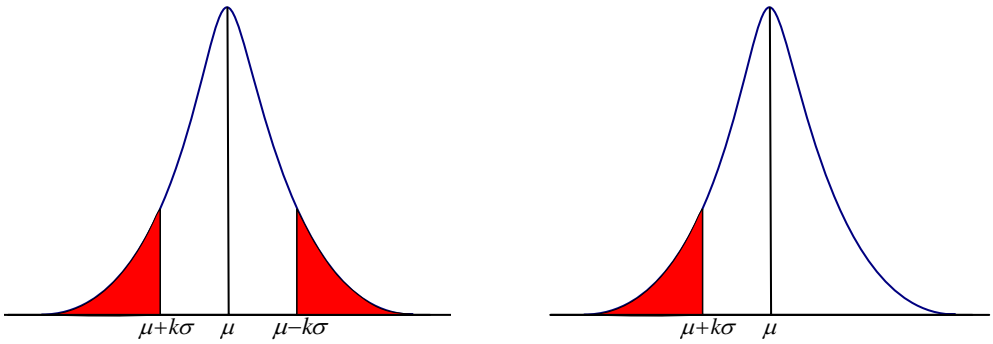

(a) Two-tailed (b) One-tailed

Figure 3.7: The white areas under the curves are the confidence intervals for the normal distribution.

Table 3.1: Chebyshev inequality evaluation, ($P(|\xi - \mu| \geq k\sigma)$ and $P(\xi - \mu \geq k\sigma)$)

k	0.1	0.5	0.9	1	1.64	1.96	2	3	4
Two-tailed (%)	(10000)	(400)	(123)	100	37.0	26.0	25	11.11	6.25
One-tailed (%)	99	80	55	50	27.0	20.7	20	10	5.88

3.2.2 Threshold updating

Brain tumors do not have any special shape or position. Therefore, a suitable way to specify the tumors is through the intensity of their pixels/voxels. In our work, the intensity of the tumor is considered a random variable with the finite mean and variance. Since the distribution of this random variable is generally unknown, the concepts of CI and CL are used to define a proper threshold for the tumor intensity.

We define the threshold in each iteration as a one-tailed interval of the accepted samples up to that iteration. We use the one-tailed interval in this definition according to our assumption that the mean intensity of the tumor region is grater than that of the non-tumor region. However, this threshold can be defined generally based on the two-tailed interval. We define an expression for threshold updating

$$T_{i+1} = \hat{\mu}_i - k\hat{\sigma}_i \qquad i \geq 0 \tag{3.14}$$

where T_{i+1} is the threshold estimation for the $(i+1)$th iteration and k is the factor which determines the confidence level and must be chosen properly. The effect of

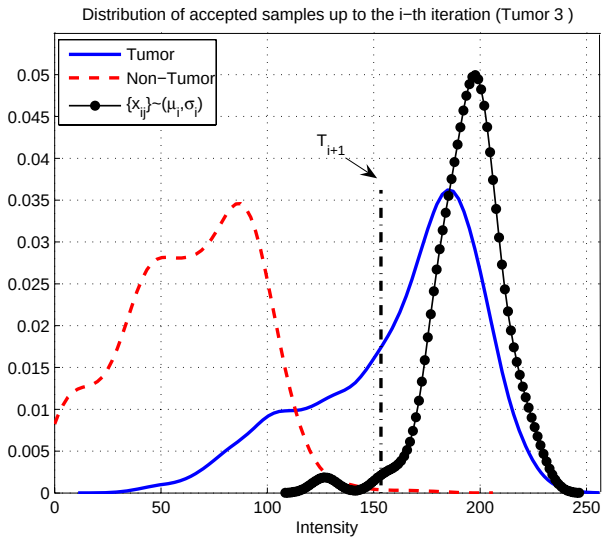

Figure 3.8: Distribution of accepted tumor samples up to the ith iteration which are a subset of tumor region. T_{i+1} is the threshold associated with $(i+1)$th iteration.

this parameter will be discussed in detail later. The mean and standard deviation, denoted by $\hat{\mu}_i$ and $\hat{\sigma}_i$, respectively, are calculated as follows:

$$\begin{aligned} \hat{\mu}_i &= \frac{1}{n}\sum_{j=1}^{n} x_{ij} \\ \hat{\sigma}_i^2 &= \frac{1}{n-1}\sum_{j=1}^{n}(x_{ij}-\hat{\mu}_i)^2 \end{aligned} \tag{3.15}$$

where $\{x_i\}$'s are the random variables representing the intensity of tumor voxels and n is the number of accepted tumor voxels up to the ith iteration. Figure 3.8 shows another real example of tumor and non-tumor distributions together with the distribution of accepted samples up to the ith iteration and the T_{i+1}. As can be seen, the set $\{x_{ij}\}$ is a subset of the tumor region.

3.2.3 Level set speed function

In this part, we discuss the challenge of determining the speed function of the level set. The original formulation of the speed function given in (3.9) does not work well when the image is noisy or when the boundary of the desired object is not clear. These characteristics are common in many MR images. In these cases, the boundary of the object is not salient enough and the image gradient information is weak. This causes the boundary leakage problem, as shown in Fig. 3.9, when we apply the level set method to detect the 3D tumor surface.

To improve the performance of the level set, the idea of integrating the region information instead of the image gradient into the level set speed function was proposed [29, 30]. Motivated by this idea, TLS uses a threshold-based speed function. The level set speed function in the ith iteration is

$$F^{(i)} = F_0.F_I^{(i)} - \epsilon\kappa_\psi \tag{3.16}$$

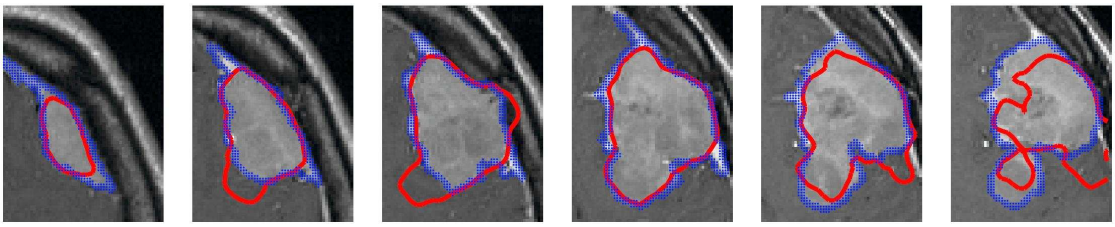

Figure 3.9: An example of boundary leaking problem of the level set method. Final result is shown in the different slices of a MR image, red curve: the detected boundary of the level set method, blue curve: the manually outlined boundary (ground truth).

where F_0 is a constant propagation determined by a positive number and $F_I^{(i)}$ is defined based on image characteristics in the ith iteration and causes the level set to finally be attracted to the tumor boundary.

Intuitively, it is desirable to have the growing speed greater in a region where the tumor likelihood is higher and vice versa. TLS uses a speed function which takes this feature into account. In other words, TLS determines $F_I^{(i)}$ for each sample proportional to its intensity difference from the threshold, so that the greater the difference the higher the speed. Let T_i be the threshold associated with the ith iteration. $F_I^{(i)}$ is defined for each sample based on its normalized intensity difference from T_i by

$$F_I^{(i)}(x,y,z) = \frac{\Delta_i}{2}\left[\frac{1+\text{sgn}(\Delta_i)}{\max(\Delta_i)} - \frac{1-\text{sgn}(\Delta_i)}{\min(\Delta_i)}\right] \tag{3.17}$$

where $\Delta_i = I(x,y,z) - T_i$ and sgn is the signum function:

$$\text{sgn}(x) = \begin{cases} 1 & x > 0 \\ 0 & x = 0 \\ -1 & x < 0 \end{cases} \tag{3.18}$$

It should be noted that the sign of $F_I^{(i)}$ indicates whether the sample is inside $(+)$ or outside $(-)$ the tumor region. In (3.17), the first and second terms give the normalized level set speed for tumor and non-tumor voxels, respectively. Such a definition benefits from the correlation among voxels in the image. For a voxel

inside the tumor region with $I(x, y, z) \geq T_i$, the larger the distance from the threshold, the higher the likelihood of being surrounded by the tumor voxels. Therefore, the level set speed function in the location of such voxels can be faster compared to the other locations. For non-tumor voxels the analysis is the same.

Consequently, $F_I^{(i)}$ has the following properties that make the zero level set converge to the tumor boundary in an iterative manner:

- $F_I^{(i)} > 0$: The zero level set is inside the tumor region and grows with the positive speed of $F^{(i)}$.
- $F_I^{(i)} < 0$: The zero level set is outside the tumor region and shrinks with the negative speed of $F^{(i)}$.

In short, this speed function helps the level set evolve and accept the voxels that are supposed to be inside the tumor while rejecting the remaining voxels. Obviously, at the tumor boundary, the speed of the level set becomes slow and the zero level set stops there; however, if the level set extends beyond the boundary and accepts non-tumor voxels, its negative speed will allow the zero level set to shrink so that it eventually coincides with the tumor boundary. Therefore, the surface of the tumor can finally be approximated by the zero level set.

3.2.4 Level set initialization

Similar to the other level set based segmentation algorithms, TLS must be initialized. The ease of initialization has always been a desirable feature of any segmentation algorithm. Since the level set method is able to handle the change of topology, our initializing surfaces do not need to be placed close to the boundaries of interest and in similar topological form. TLS uses a small sphere inside the tumor as the initial zero level set to start the surface detection. Initialization for TLS is done in the tumor region, from which we obtain the first estimate of the threshold, T_1.

We define the reference slice as the one that includes a relatively large tumor cross-sectional area compared to the other slices. It should be noted that the choice of this reference slice will not affect the end result. A volume of interest is selected manually and the whole computation is performed inside it to reduce the computational time of the algorithm. However, by using a more effective method the need for the volume of interest is removed and the algorithm becomes more automatic. This effective method is discussed in the next chapter.

Depending on the convexity or concavity of the tumor shape the complexity of initialization varies. For convex tumor shapes, the initial zero level set is a spherical surface whose center is at the center of the tumor region in the reference slice. (A body is convex if, for any pair of points inside the body, the line segment

which joins them lies entirely in it; otherwise the body is concave [40].) For simple tumor shapes whose cross-sections at the reference slice are in the central portion of the image, the center of the sphere is placed automatically at the center of the reference slice. Such an initialization ensures that the area of intersection of this sphere with the reference slice lies entirely within the tumor region. However, it is not necessary for the other slices to satisfy this condition. T_1 is calculated using the tumor voxels in the area of intersection (3.14, with a proper value for k that is discussed in section 3.3.1)

Now the signed distance function ψ at $t = 0$ can be expressed as

$$\psi(i, j, k, t = 0) = (i - x_c)^2 + (j - y_c)^2 + (k - z_c)^2 - r^2 \tag{3.19}$$

where (x_c, y_c, z_c) denotes the coordinates of the sphere center, and r the radius of it. It is clear that ψ has the positive value outside the initial surface, and negative inside. This makes the evolving front deform from inside the tumor to the desired tumor surface as we expected. The coordinates of the sphere center, x_c, y_c and z_c, are determined by

$$x_c = D_x/2, \quad y_c = D_y/2, \quad z_c = \text{Reference slice number} \tag{3.20}$$

where D_x, D_y stand for the volume of interest dimension along x and y axis,

respectively. Figure 3.10 illustrates the initial surface and its corresponding 2D curves in the cross-sectional images.

The initialization for concave tumors is slightly more complicated since a single sphere may fail to detect all the desired boundaries due to the complex tumor shape. Moreover, it may take large number of iterations for a single sphere to reach the boundaries of the concave tumor because of the need for the topology changes. As shown in Fig. 3.11, in the first row after 40 iterations the level set cannot reach the tumor regions in the 3th and 4th slices, and in the second row an intuitively acceptable result is achieved after 60 iterations, but, the upper left corner of the tumor in the 6th slice and a part of tumor in the 11th slice still are not reached.

Therefore, in such cases multiple spheres may be required for higher segmentation accuracy with fewer iterations. Figure 3.12 shows an example of such an initialization in the concave tumor. It should be noted that the reference slice cross section requirement must also be met in this situation. As mentioned before,

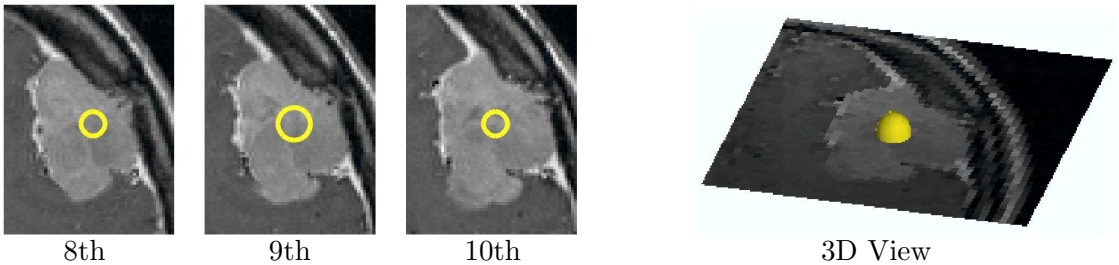

Figure 3.10: Initialization of the level set method by automatically putting a small sphere ($r = 5$ voxels) at the volume of interest center in 9th slice.

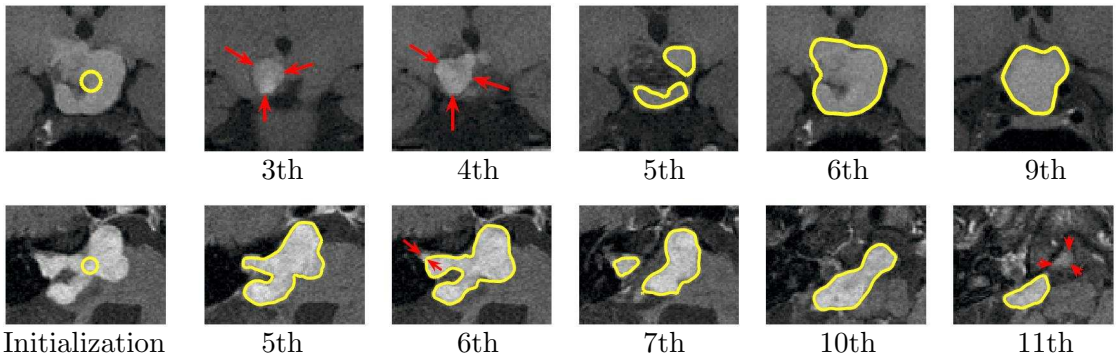

Figure 3.11: Limitation of the single sphere initialization, failure to detect the whole desired tumor surface. First row: Tumor 6, (T1-pre contrast, $256 \times 256 \times 12$, tumor-contained slices: 3th-9th), Second row: Tumor 3, (T1-post contrast, $256 \times 256 \times 11$, tumor-contained slices: 2th-11th).

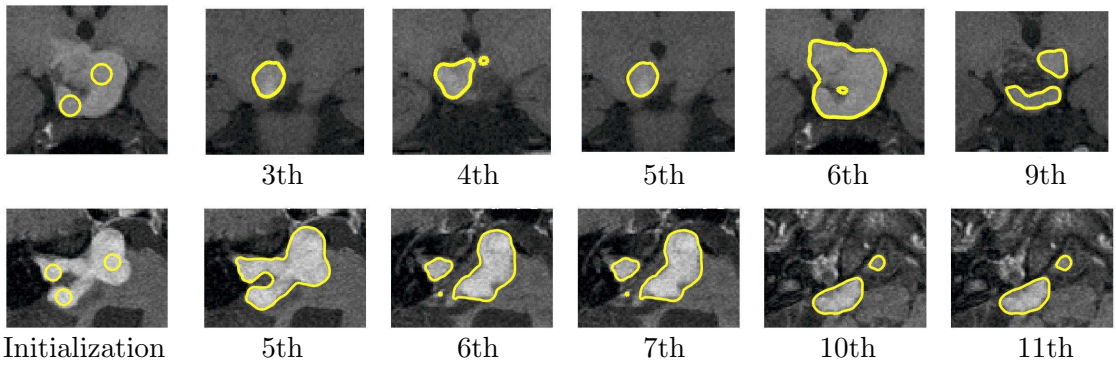

Figure 3.12: Improved segmentation results obtained by the multiple spheres.

this cross section requirement is only for the reference slices and not for the other slices. As Fig. 3.13 shows, during the initialization for tumor 3, one of the initial spheres crosses over the tumor boundaries, in the 7th slice, to the background. In such cases, as expected, that part shrinks and finally is attracted to the desired boundaries according to the properties of the new speed function F.

In the concave tumors, choice of the initial sphere positions affects the final

6th 7th

Figure 3.13: Level set initialization in Tumor 3. Sphere, shown with arrow, crosses over the tumor boundary to the background.

result more significantly compared to the case of convex tumors. Therefore, the spheres should be chosen independently and evenly distributed across the entire tumor region. In fact, higher convergence speed and better precision in the final results can be achieved by suitable initialization. Figure 3.14 demonstrates the merging effect of the evolving spheres.

The TLS algorithm is robust with respect to initialization; however, properly accomplishing it results in a higher convergence rate and better accuracy in the final result. To determine the effects of initialization on the final algorithm results, we move the center of the initial sphere inside the convex tumor in the reference

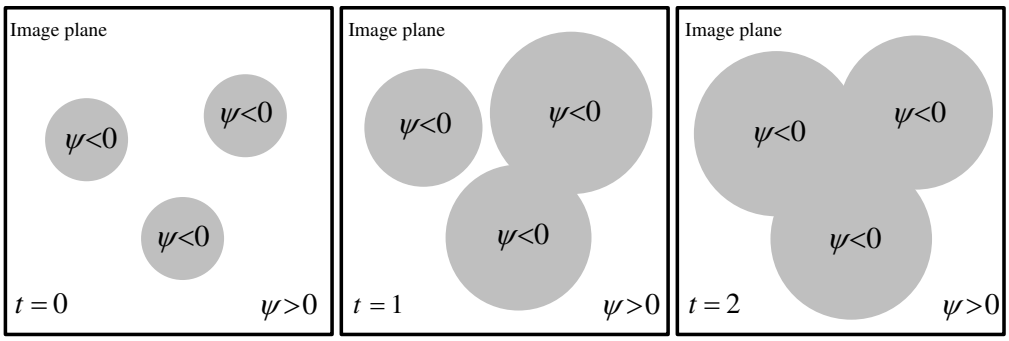

Figure 3.14: Merging of three spheres when evolving with constant speed along normal direction.

slice, and for each center position, adaptive TLS extracts the tumor surface and a threshold curve is obtained.

Figure 3.15 shows the mean threshold curve and the threshold deviation at each iteration resulting from 40 different initializations in one convex tumor. It can be seen that as the iteration number increases, the threshold deviation decreases so that in the last few iterations the deviations are almost zero. Since the segmentation results are dependent on the threshold value, this is a demonstration of algorithm robustness to initialization. For concave tumors, the convergence rate of the algorithm is more affected by initialization, but, the final results are the same.

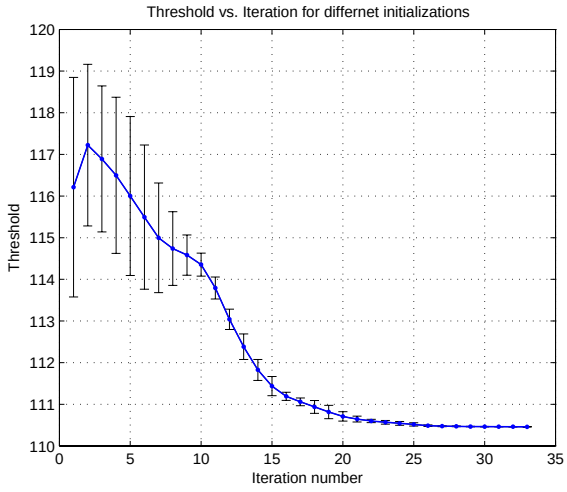

Figure 3.15: Deviation of threshold for different initializations inside the tumor region. The deviations in the final iterations are very small.

3.2.5 Stopping criterion

As described, TLS updates the threshold at each iteration based on the accepted tumor samples up to that point. At the tumor boundary, the negative speed of the level set for non-tumor samples causes TLS to reject them. Therefore, the rate of accepting new samples declines and the variation of the threshold will become negligible per iteration. Figure 3.16 shows the variation of threshold versus iteration for a real image.

The stopping window of length W_s is defined such that it contains the thresholds associated with the last W_s iterations. TLS stops when, for t_s consecutive iterations, the variance of the threshold values in the stopping window becomes less than a small number ε. The parameter t_s is defined to prevent stopping at

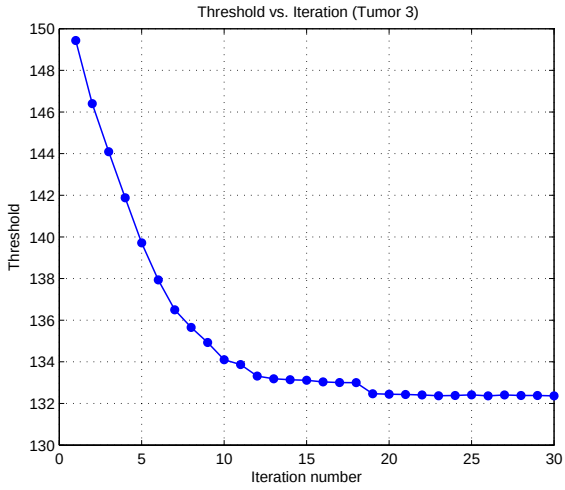

Figure 3.16: Variation of the threshold in different iterations. The threshold remains almost unchanged in the last iterations.

a local minimum since the threshold curve is not necessarily decreasing and noise may cause some local minima. Therefore, the triple (W_s, t_s, ε) determines when the algorithm stops. For example, for triple $(5, 3, 0.02)$ the algorithm stops where the variance of the last five threshold values becomes less than 0.02 for 3 consecutive iterations. Suitable values of these three parameters are obtained experimentally.

3.3 Analysis

In this section, we describe the procedure for threshold updating and the modified TLS for segmentation of non-homogeneous tumors. The robustness of the algorithm with respect to initialization is also discussed and the values of some user defined parameters such as F_0, ϵ, radius of the initial sphere, r, and narrow band width, NB, are proposed.

3.3.1 Threshold updating parameter

The convergence rate of the algorithm and the accuracy of segmentation are directly related to the choice of the threshold, which is also determined by k. For a small value of k, the level set may never grow while for a relatively large value of k, convergence of TLS may not be possible. We propose two different schemes for choosing an appropriate value of k. In the first, search-based, scheme the value of k is kept fixed during the level set evolution process, while in the second, adaptive,

scheme, it is chosen adaptively as the level set evolves. The latter scheme, though, requires a slightly more complicated initialization to reduce the overall complexity of the algorithm.

The search-based scheme finds the best possible value of k by searching an interval of feasible values. From (3.13), the smallest value of k which still can provide an acceptable confidence level of 50% for the samples, is $k = 1$. Therefore, this value can be used as the lower bound of k in the following analysis. Now, take k to be a relatively large value so that the threshold becomes very small. It is obvious that in such a case, TLS never converges because the samples of non-tumor region will be included in the level set evolution process. Therefore, there must exist a critical value of $k_c \geq 1$, beyond which TLS diverges. Since TLS achieves its best performance at k_c, the main goal of the search-based scheme is to find an approximation of it. For this reason, the values of k, such that $k \geq 1$, are swept with a reasonably small step of s_k. It should be noted that s_k decides the trade-off between the accuracy and speed of this search.

The search-based scheme is simple, but an exhaustive search must be performed in order to find k_c. The adaptive scheme removes the search complexity by an additional sampling from the non-tumor region in the initialization phase. Such a sampling, although requiring more user involvement, greatly reduces the complexity of the computation. The shape of the selected area in the non-tumor region is not important but must not contain any tumor voxels. Preferably, it should be

selected close to the tumor boundary where the tumor and non-tumor intensities are more correlated (Fig. 3.17). In the adaptive scheme, the value of k is modified adaptively as the algorithm progresses. To define a proper value of k_i in each iteration, the confidence interval of tumor samples along with the confidence interval of non-tumor samples is used.

If we assume that the intensities of tumor and non-tumor regions are separated, their confidence intervals are also separated, so that we have

$$\hat{\mu}_{NT} + k_{NT}\hat{\sigma}_{NT} \leq \hat{\mu}_i - k_i\hat{\sigma}_i \tag{3.21}$$

where $(\hat{\mu}', \hat{\sigma}')$ are the mean and standard deviation associated with the non-tumor samples. The goal is to find the largest possible value of k_i so that the confidence intervals of tumor and non-tumor samples do not overlap, and in the worst case $\hat{\mu}' + k'\hat{\sigma}' = \hat{\mu}_i - k_i\hat{\sigma}_i$. Moreover, since our confidence about the tumor and non-tumor samples is similar, the same confidence level is considered for both tumor and non-tumor samples in each iteration ($k' = k_i$). Therefore, a proper approximation

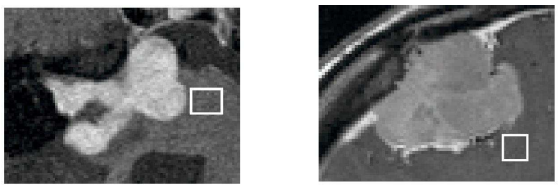

Tumor 3 Tumor 13

Figure 3.17: Initialization inside the non-tumor region near to the tumor boundary where the intensities are closer to those for the tumor.

of k_i can be found by

$$\begin{aligned} \hat{\mu}_{NT} + k_i\hat{\sigma}_{NT} &= \hat{\mu}_i - k_i\hat{\sigma}_i \\ \Rightarrow \qquad k_i &= \frac{\hat{\mu}_i - \hat{\mu}_{NT}}{\hat{\sigma}_i + \hat{\sigma}_{NT}} \end{aligned} \tag{3.22}$$

Based on (3.22), the values of k_i are proportional to the intensity level difference between the tumor and background. The higher the difference in intensity levels, the greater the value of k_i, which means a higher confidence level around the tumor samples.

3.3.2 Modified TLS

The algorithm that we have introduced is appropriate for homogeneous tumors because, in the threshold updating procedure, all accepted tumor samples up to each iteration are used. We introduce minor modifications to the threshold updating procedure so that TLS would be able to segment non-homogeneous tumors. First, $(\hat{\mu}_i, \hat{\sigma}_i)$ in each iteration is calculated using only the accepted tumor samples that are greater than the threshold value of the previous iteration, T_i:

$$\begin{aligned} \hat{\mu}_i &= \frac{1}{n}\sum_{x_{ij}>T_i} x_{ij} \\ \hat{\sigma}_i^2 &= \frac{1}{n-1}\sum_{x_{ij}>T_i} (x_{ij} - \hat{\mu}_i)^2 \end{aligned} \tag{3.23}$$

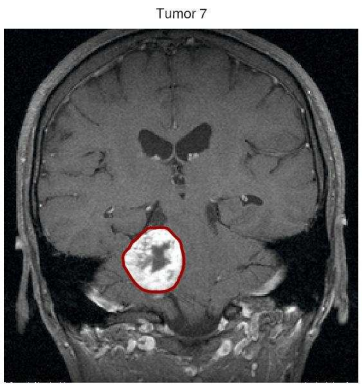

Figure 3.18: Modified TLS result in the reference slice of non-homogeneous tumor.

Second, the initial level set should not contain any sample from the non-homogeneous region. These modifications, along with the effect of the smoothness parameter in the level set speed function, enables TLS to segment the non-homogeneous tumors. Figure 3.18 shows an example of the tumor that has been successfully segmented by the modified TLS.

3.3.3 Parameter setting

In this section, we propose the values of the parameters in the level set equation that should be set by the user. For solving the level set equation, a discrete Cartesian grid is used to compute a numerical approximation of the solution. The grid size is chosen based on the voxel resolution of the corresponding MR image. In such a case, the smallest unit of measure on the grid is the cell size denoted by $\{\Delta x, \Delta y, \Delta z\}$. Since the level set can only grow on this grid, the radius of the initial

sphere must be larger than $\min(\Delta x, \Delta y, \Delta z)$. We set it to $r = 2\min(\Delta x, \Delta y, \Delta z)$. Choosing this value for the sphere radius leads the front curvature, κ_ϕ, to be of the order of $O(1/\min(\Delta x, \Delta y, \Delta z))$ [24]. Moreover, in the level set speed function, $F_0 F_I$ decides the level set speed while $\epsilon\kappa_\phi$ prevents the level set from trapping into the noisy structures that are inside the tumor region. Therefore, the parameter $\epsilon\kappa_\phi$ must be smaller than $F_0 F_I$ so that it does not affect the level set evolving direction; for example, we select $\epsilon = 0.5\min(\Delta x, \Delta y, \Delta z)$ and $F_0 = 2$. The length of the narrow band around the zero level set is selected equal to the maximum dimension of a voxel, i.e., NB $= \max(\Delta x, \Delta y, \Delta z)$, and the stopping criterion parameters are experimentally set as $(5, 3, 0.02)$.

3.4 Test results and discussion

In this section, we compare the performance of search-based and adaptive TLS and show the segmentation results. The test dataset contains tumors of different shapes, locations, sizes, intensity, and enhancement. In the following the specifications of the available dataset are described.

3.4.1 Image acquisition

The dataset, shown in Fig. 1.3, contains the MR images of 16 patients that were acquired at the Singapore National Cancer Center. All the patients were imaged

on a 1.5T MR scanner using a standard clinical imaging protocol to obtain T1-weighted (T1) and contrast enhanced T1 (gadolinium enhanced) images. Each MR image has an in-plane resolution of 256×256, field of view of 160-240 mm, and slice thickness of 2-3 mm. For the 3 mm slices, linear interpolation is used to obtain higher inter-slice resolution of 1.5 mm and decrease the uncertainty between slices. Among these MR images, 6 tumors, labeled from 1 to 6, are concave and the other tumors, labeled from 7 to 16, are convex. An experienced radiologist manually segmented the tumors to obtain the ground truth, GT, for validation of segmentation results.

3.4.2 Search-based scheme vs adaptive scheme

The performance of the search-based and adaptive algorithms are compared for the concave (Tumor 3) and convex (Tumor 13) tumors (Fig. 3.17). In the search-based scheme, parameter k sweeps the feasible values with the step size of $s_k = 0.1$ to estimate k_c.

Figure 3.19 shows the variation of threshold versus iteration number for some values of k in the search-based TLS and for both convex and concave tumors. In both figures, when k is larger than certain values, the algorithm diverges, which enables us to obtain k_c equal to 1.7 and 2 for the convex and concave cases, respectively. The greater value of k_c for Tumor 3 is expected because of the higher

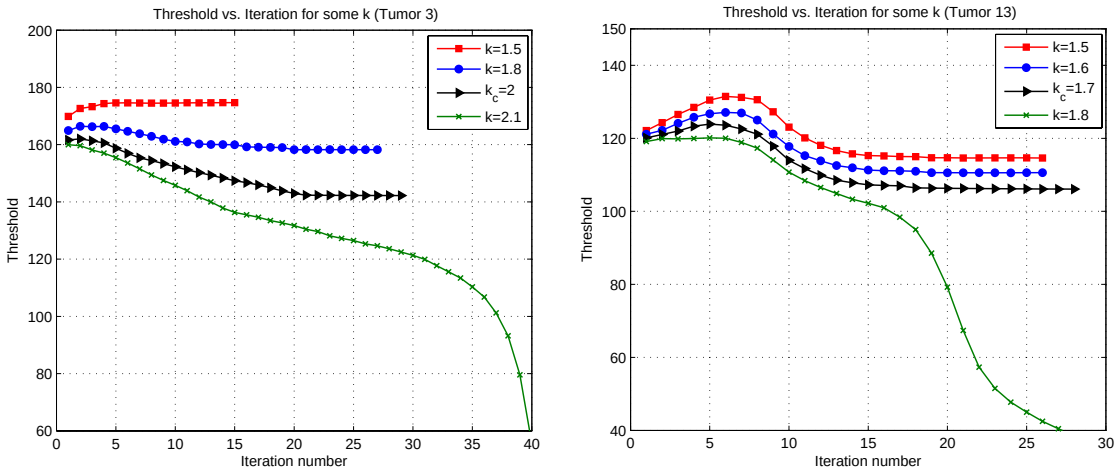

Figure 3.19: Variations of threshold vs. iteration number for some values of k and for two different tumor types. (left) concave tumor, $k_c = 2$ (right) convex tumor, $k_c = 1.7$.

difference in intensity level between the tumor and non-tumor regions. It should be noted that in these two cases, for small values of k, the threshold first starts to increase and, then, after some iterations, decreases toward its final value. This is due to the existence of non-tumor voxels inside the initialized sphere which belong to non-reference slices. Consequently, the level set shrinks to discard such voxels before growing inside the tumor region. For smaller values of k, the duration of this shrinking is longer.

For the adaptive TLS, the variations of k versus iteration number for the same tumors are shown in Fig. 3.20. The values of parameter k are also higher for Tumor 3, which is consistent with the search-based results. Another observation is that the value of k_i for both cases decreases to an almost constant value. The

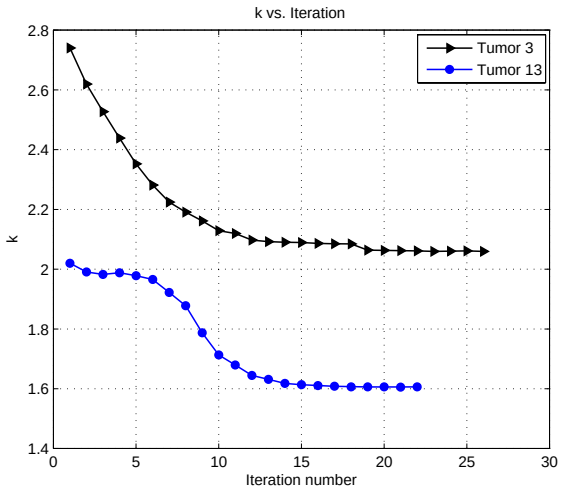

Figure 3.20: Variation of k vs. iteration number in adaptive scheme and for two different tumor types.

reason is because, by growing the level set and increasing the standard deviation of accepted tumor samples, $\hat{\sigma}_i$, the value of k_i from (3.22) decreases until the level set reaches the tumor boundary. At this stage, the mean and standard deviation of the tumor set remain unchanged, which results in an almost constant k_i in the last few iterations. Interestingly, the final values of k_i in both cases are close to their corresponding k_c obtained from the search-based TLS.

Finally, comparing the threshold variation curves associated with both search-based and adaptive schemes (Fig. 3.21), we may conclude that the convergence rate of the adaptive scheme is higher than that of the search-based scheme. This is explained by the additional knowledge extracted from the non-tumor samples in the adaptive scheme.

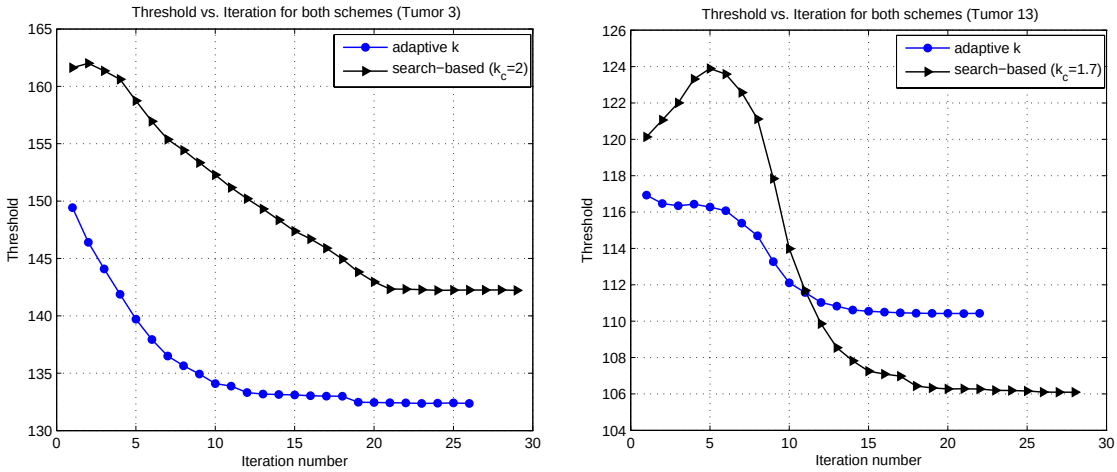

Figure 3.21: Comparison between threshold variation for search-based and adaptive schemes and for two different tumor types.

3.4.3 Segmentation results

We apply TLS algorithm to our dataset to test if it works correctly. Figure 3.22 shows the final segmentation results by adaptive TLS on some of the MR images. The final 3D shapes are shown in the right-most column, and the cross-sections of these extracted tumor surfaces with some of the image slices are shown in the five other columns. The subjective comparison between these segmentation results and the ground truths indicates a good agreement between them. However, the objective evaluation provides us with better assessment of the algorithm performance. For this purpose, the results of 3D tumor segmentation by TLS for both search-based and adaptive schemes are compared with the ground truths via some quantitative evaluation methods. Details of these methods and the comparison results are given in Chapter 5.

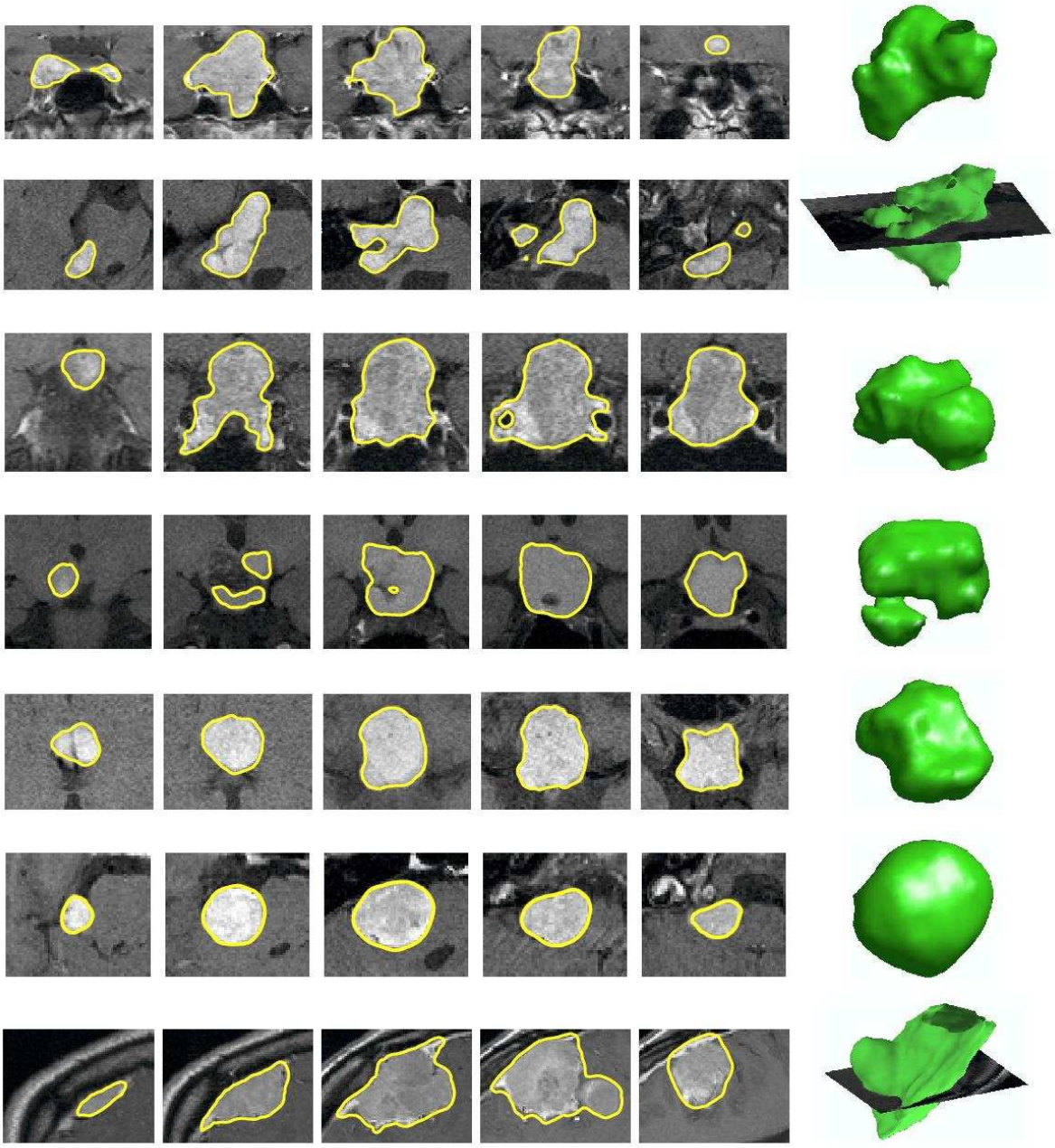

Figure 3.22: The final segmentation results using adaptive TLS approach. The indexes of tumors from top to bottom are: 2, 3, 5, 6, 8, 11 , and 13. First five columns are some cross-sectional images of the 3-D tumors in the last column.

3.5 Summary

This chapter presents a new threshold-based approach called TLS for 3D tumor segmentation in the brain MR images. TLS uses the level set as a deformable model and defines its speed function based on intensity thresholding so that no explicit knowledge about the density functions of the tumor and non-tumor regions are required. In this approach, we replace the requirement of selecting the threshold by the requirement of selecting the algorithm parameter, k in order to propose an iterative process. By defining the threshold based on the notion of confidence interval, we introduce an iterative scheme for updating the threshold. Therefore, the threshold is updated iteratively throughout the level set growing process using either a search-based or adaptive scheme. Our test with various initializations shows that this algorithm is robust so that the level set can grow into the entire tumor in all cases.

The TLS method can segment a variety of tumors as long as the intensity difference between tumor and non-tumor regions in each case is sufficiently large (tumor regions can be distinguished by eyes). Moreover, the TLS performance is better where the level of this intensity difference is higher. This method does not require the information from both pre- and post-contrast MR images and only one of these image sets is sufficient. TLS can segment both concave and convex tumors, although its performance is better for convex ones. In the cases of con-

cavity, good initialization can result in better segmentation. Moreover, tumors with non-homogeneous intensities can also be segmented using modified TLS, if the non-homogeneity is inside the tumor region. The visualization and subjective evaluations of the segmentation results demonstrate the effectiveness of our proposed approach.

Chapter 4

SVM-based 3D Tumor Segmentation Using Level Set Method

In the previous section, we have developed the TLS algorithm based on the level set with region information integrated to detect the 3D tumor surface in the MR images. Using the proposed approach, the user involvement is reduced greatly and the experiments have shown its effectiveness. However, there are still some difficulties due to the necessity of non-tumor sampling in adaptive scheme as well as computational expense of search-based scheme. This chapter tries to address these problems by developing a new density-independent segmentation scheme.

Avoiding density estimation, the supervised classification techniques can be efficiently used for tumor segmentation. Among such techniques, the support vector machine, SVM, approach has the ability of learning the nonlinear distributions of

tumor and non-tumor data without additional prior knowledge. Two-class SVM classifies data using training samples from both tumor and non-tumor regions. However, with some modifications in the SVM approach, a new one-class SVM has been proposed [41]. This one-class family formulates the tumor segmentation in the form of one-class classification problem so that the positive training samples are only used in its learning process.

The advantage of one-class SVM is that it outperforms the two-class scheme in the cases of unbalanced data whenever it is provided with sufficient training samples [9]. However, it is known that tumors may have non-uniform intensities and noisy structures. In such cases, the training set of one-class SVM must be large enough in order to possess most of the tumor features, otherwise the result is unstable and dependent on the initial set. Generally, having such a training set is not easy and needs more user interaction.

In this chapter, a one-class SVM-based algorithm is introduced that benefits the level set for 3D tumor segmentation in MR images. This method addresses the problem of acquiring proper training set through an iterative basis. Knowing the advantage of one-class SVM in handling the nonlinear distributions without additional prior knowledge, we design a speed function for the level set. In order to train the SVM, the samples inside the zero level set are used and the training set is iteratively refined as the level set grows. The iterative process continues until the level set reaches the tumor boundary and the stopping criterion is met.

One merit of our method is that it uses the small set of initialization as SVM basic training set and enables SVM to finally learn the nonlinear distribution of the tumor via iterations. Therefore, this approach also addresses the shortcoming of TLS algorithm by reducing the user involvement. The level set initialization phase in this approach is completely the same as that of the TLS approach. We examined our method on several clinical MR images and the experiments demonstrate that the segmentation results by this approach is comparable with the TLS results.

4.1 SVM method

Support vector machine (SVM) comprises a new class of learning algorithm, motivated by results of statistical learning theory [42, 43]. Originally developed for pattern recognition, SVM represents the decision boundary in terms of a typically small subset of all training examples, called the support vectors [44]. SVM is primarily used for binary, one-class, and n-class classification problems. It combines linear algorithms with non-linear kernel functions which makes it a powerful tool in the machine learning community. The most important features of SVM are [45]:

- One parameter to control the trade-off between generalization and complexity (in the standard version).
- Few training parameters (one regularization plus some kernel parameters).

- An excellent classification performance compares to other approaches for example neural networks and polynomial classifier.

- Fast application time.

The simplest model of SVM is the so-called hard margin or maximal margin classifier [46]. In this model, the SVM training aims to find the best generalizing hyperplane, which is the hyperplane with maximal margin, to separate the two classes. Since the samples may not always be linearly separable, the optimization problem can be modified to enable SVM to classify non-linear data distributions. For this purpose, the data can be implicity transformed to a non-linear feature space, in which a separation might be possible. There exist also modifications of SVM to apply it to unlabeled data. This approach is know as one-class SVM. In the followings, more detailed descriptions of two-class and one-class SVM are provided.

4.1.1 Two-class SVM

As mentioned, the SVM finds the best hyperplane that separates the two classes, however, it might not be always possible to have such a hyperplane. Therefore, a non-linear preprocessing, Φ, can be applied to map the patterns to a high dimensional feature space, Γ, in which a linear separation is feasible. Figure 4.1 shows a simple model of this non-linear preprocessing. By going into a high dimensional

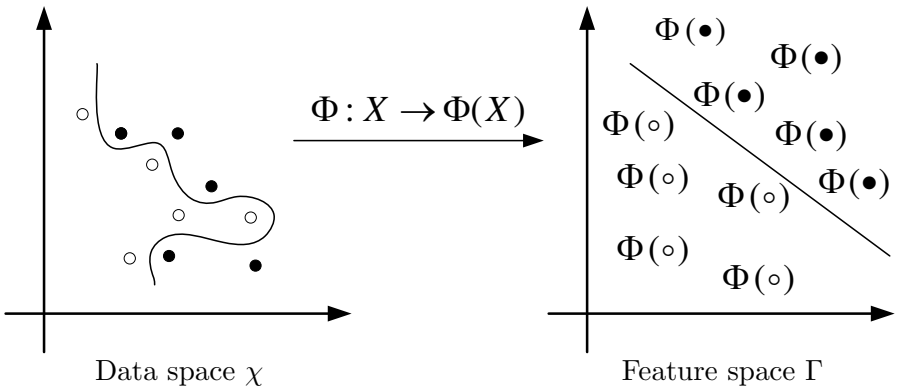

Figure 4.1: Each data point is mapped by a non-linear function from data space to a feature space.

space, function of a low complexity (e.g., hyperplane) might be sufficient to solve the classification problem. Moreover, since SVM finds the hyperplane with maximal margin, the generalization performance is preserved even in high dimensional feature space.

Given a non-linearly separable dataset with N samples, $\chi = \{\mathbf{x}_i\}_{i=1}^{N}$ labeled as $y_i = \pm 1$, we want to classify this dataset into two classes. Since it is difficult to separate these two classes in the input space directly, they are mapped into a higher dimensional space, $\chi' = \{\mathbf{x}'_i = \Phi(\mathbf{x}_i)\}_{i=1}^{N}$. The separating hyperplane H in the feature space is described by the weight vector $\mathbf{w}$ and the bias b. Therefore, a pattern $\mathbf{x}_i$ is classified as follows:

$$\langle \mathbf{w}.\mathbf{x}'_i \rangle + b \begin{cases} < 0 & \Rightarrow \mathbf{x}_i \in \Omega^- \\ > 0 & \Rightarrow \mathbf{x}_i \in \Omega^+ \end{cases} \tag{4.1}$$

Since the data may not still be linearly separable in feature space, the optimization problem of the hard margin classifier cannot be solved. Therefore, we allow the margin constrains to be violated by introducing a slack variable $\xi_i \geq 0$. The introducing of the slack variable leads to the following primal optimization problem for the soft margin classifier:

$$\begin{aligned} \min_{\mathbf{w},\xi} \quad & \frac{1}{2}\langle \mathbf{w}.\mathbf{w} \rangle - C\|\xi\| \\ \text{subject to} \quad & y_i(\langle \mathbf{w}.\mathbf{x}_i' \rangle + b) \geq 1 - \xi_i \quad , \quad \xi_i \geq 0 \end{aligned} \tag{4.2}$$

The term ξ_i measures how far $\mathbf{x}_i'$ lies on the wrong side of the class border. The regularization parameter $C \geq 0$ controls the tradeoff between maximizing the margin of the hyperplane and minimizing the sum of margin error, that means the sum of distances of how far the training samples $\{\mathbf{x}_i'\}$ lie outside the class border.

This optimization problem cannot be solved directly and it should be transformed to the dual optimization problem.

$$\begin{aligned} \max_{\alpha} \quad & W(\alpha) = \sum_i \alpha_i - \frac{1}{2}\sum_{i,j} \alpha_i \alpha_j y_i y_j \left(\langle \mathbf{x}_i'.\mathbf{x}_j' \rangle + C^{-1}\delta_{ij} \right) \\ \text{subject to} \quad & \sum_i y_i \alpha_i = 0 \quad , \quad \alpha_i \geq 0 \end{aligned} \tag{4.3}$$

Instead of minimizing the primal optimization problem, maximization of the equivalent dual function is preferable since the vector $\mathbf{x}_i'$ only appear as part of an inner

product $\langle \mathbf{x}'_i.\mathbf{x}'_j \rangle$ that is the prerequisite for the application of kernel function. During the maximization process, most of the $\{\alpha_i\}$'s become zero, the rest are the *support vectors*.

The solution for $\mathbf{w}$ of the optimization problem is derived as

$$\mathbf{w} = \sum_i \alpha_i y_i \mathbf{x}'_i \tag{4.4}$$

Having this value for $\mathbf{w}$, the bias b can be calculated. Finally, with the solution for $\mathbf{w}$ and b, a new pattern $\mathbf{x}$ can be classified. The margin function is given by

$$\begin{aligned} f(\mathbf{x}) &= \langle \mathbf{w}.\mathbf{x}' \rangle + b \\ &= \sum_i \alpha_i y_i \langle \mathbf{x}'_i.\mathbf{x}' \rangle + b \end{aligned} \tag{4.5}$$

The decision function $d(f(\mathbf{x}))$ is often defined as

$$d(f(\mathbf{x})) = \mathrm{sgn}(f(\mathbf{x})) \tag{4.6}$$

Kernel Trick

The learning ability of SVM originates from the kernel trick [41]. Both the dual objective function (4.3) and the margin function (4.5) have a remarkable property that the data appears only inside the inner product. Thus it is not necessary to

declare Φ explicitly and it is sufficient to introduce a kernel function K that is defined as the inner product of two transformed input vectors:

$$K(\mathbf{x}_i, \mathbf{x}_j) = \langle \Phi(\mathbf{x}_i)\Phi(\mathbf{x}_j) \rangle = \langle \mathbf{x}'_i . \mathbf{x}'_j \rangle \tag{4.7}$$

Replacing the inner product $\langle \mathbf{x}'_i . \mathbf{x}'_j \rangle$ by a kernel function $K(\mathbf{x}_i, \mathbf{x}_j)$ leads to the optimization of the hyperplane in the feature space Γ and realizes a nonlinear discrimination function in input space. Therefore, (4.5) can be expressed as follows:

$$f(\mathbf{x}) = \sum_i \alpha_i y_i K(\mathbf{x}_i, \mathbf{x}) + b \tag{4.8}$$

Several kernel functions have been proposed for the support vector classifier. Commonly used kernels are summarized as follows [45]:

- RBF kernel:

$$K(\mathbf{x}_i, \mathbf{x}_j) = \exp\left(-\frac{\|\mathbf{x}_i - \mathbf{x}_j\|^2}{2\sigma^2}\right) \tag{4.9}$$

- Polynomial kernel:

$$K(\mathbf{x}_i, \mathbf{x}_j) = (\langle \mathbf{x}_i . \mathbf{x}_j \rangle + c)^d \tag{4.10}$$

- Sigmoid kernel:

$$K(\mathbf{x}_i, \mathbf{x}_j) = \tanh(k\langle \mathbf{x}_i . \mathbf{x}_j \rangle - \delta) \tag{4.11}$$

- Linear kernel:

$$K(\mathbf{x}_i, \mathbf{x}_j) = \frac{\langle \mathbf{x}_i . \mathbf{x}_j \rangle}{\sigma}. \tag{4.12}$$

It should be noted that these kernels are not equally useful. Among them, the preferable choice is the RBF kernel [41]. Using the kernel trick, SVM can deal with nonlinear multi-mode data distribution.

4.1.2 One-class SVM

The methods developed for support vector machines for binary classification can be modified for a one-class classification. One-class SVM constructs a classifier only using a set of labeled positive patterns, $\chi = \{\mathbf{x}_i\}_{i=1}^{l}$, called positive training samples [41]. As before, consider there is a feature map that maps the training data into a higher dimensional space, i.e. $\Phi : \chi \rightarrow \Gamma$. One-class SVM minimizes an objective function as follows:

$$\begin{aligned} \min_{\mathbf{w}\in\Gamma, \xi\in\mathbb{R}^l, b\in\mathbb{R}} \quad & \frac{1}{2}\|\mathbf{w}\|^2 + \frac{1}{\upsilon l}\sum_i \xi_i - b \\ \text{subject to} \quad & (\mathbf{w}.\Phi(\mathbf{x}_i)) \geq b - \xi_i \quad , \quad \xi_i \geq 0 \end{aligned} \tag{4.13}$$

We expect the decision function $f(\mathbf{x})$ to be positive for most of $\{\mathbf{x}_i\}$ contained in the training set, while the term $\|\mathbf{w}\|$ is small. The actual trade-off between these two goals is controlled by the regularization term $\upsilon \in (0, 1]$ [44]. The smaller υ

is the more trained samples will be included by the hyperplane. Once the optimal values of these training parameters are obtained, test data can be classified according to the following decision function.

$$f(\mathbf{x}) = \text{sgn}\left(\sum_i \alpha_i K(\mathbf{x}_i, \mathbf{x}) + b\right) \tag{4.14}$$

The learning ability of one-class SVM also originates from the kernel tricks and as it was mentioned, the widely used kernel is the RBF kernel, (4.9). The parameter σ^2 in this equation is the kernel width. If M denotes the number of support vectors obtained through the learning process, and d_{max} shows the maximum distance between these support vectors, the parameter σ^2 can be calculated as follows:

$$\sigma^2 = \frac{d_{max}^2}{2M} \tag{4.15}$$

This ensures that the RBF kernel is neither too peaked nor too flat; both of these two extreme conditions should be avoided. For a large training sets, this simple approach gives reasonable results [46].

In tumor segmentation, the focus is to separate tumor data (positive samples) from non-tumor data (negative samples). Therefore, the problem is a two-class classification, since, we can consider the tumor and non-tumor data as two separate classes. In conventional two-class classification, the data from both classes are

available and the decision boundary is supported from both sides. Most of the classifiers assume almost equally balanced data classes and do not work well when one class is under-sampled or completely absent.

An illustration of undesirable classification result reached by two-class SVM is given in Fig. 4.2. In this figure, the decision boundary generated by two-class SVM is based on the training sample indicated by '$\circ$' and '$\bullet$'. The circle around the target data is the decision boundary produced by one-class SVM. It is obvious that two-class SVM has misclassified a large part of nontarget data (indicated by dot) into target data, while one-class SVM performs well in separating target data from others. Therefore, as this figure shows, under-samples nontarget data would result in unacceptable segmentation accuracy by two-class SVM.

In tumor segmentation, to achieve a satisfied segmentation result by using two-class classifiers, user must be able to figure out the distribution of tumor and non-tumor data. It implies an extra task that the user should have additional prior knowledge about the data classes. Failure to do this usually results in under-sampled data, and thus leads to unsatisfied segmentation results. These disadvantages make the conventional two-class segmentation systems unpractical. Therefore, we argue that the tumor segmentation issue could be formulated as a one-class learning problem and accordingly propose a new segmentation approach based on one-class SVM.

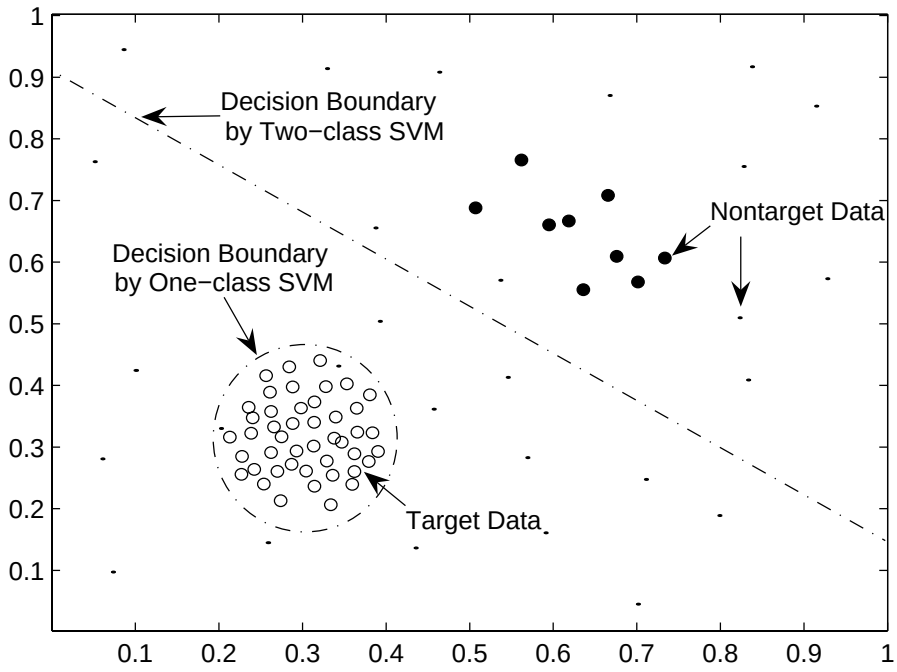

Figure 4.2: Undesirable classification result by two-class SVM. '○' indicates the target sample for training; '●' indicates the nontarget samples for training. '.' and '●' indicate the distribution of non-target data. Two-class SVM is trained on the samples indicated by '○' and '●'. One-class SVM in trained only on the samples indicated by '○'.

4.2 SVM-based segmentation by level set

In the proposed TLS approach (described in the previous chapter), we assumed that the histogram of tumor and non-tumor regions are slightly overlapped. Considering the same assumption here, we have two regions that are nonlinearly separable (by projecting to the higher dimensional feature space). Therefore, two-class SVM can be used to estimate the distribution of these two classes and classify them. But, estimating the distribution of non-tumor region is difficult due to its non-uniform intensities. This difficulty may lead to under-sampling of non-tumor region

and thus unsatisfied classification results. To get rid of non-tumor distribution estimation, the problem of tumor segmentation can be formulated as a one-class classification problem along with the decision boundary extraction.

As we know, having appropriate features of tumor region, one-class SVM can automatically learn the actual tumor distribution without any prior knowledge. In the proposed method, the classification part is performed using one-class SVM and then the level set is grown on this classified data to extract the tumor surface. For simplicity, when we use SVM in the remaining of this chapter, it implies one-class SVM.

Since in most of the cases, tumors also have non-uniform intensities, SVM cannot result in good classification using a small training set as well as the classification result is dependent on the training set. On the other hand, the selection of a large training set may increase the user interaction. The proposed method addresses this trade-off using an iterative approach. Figure 4.3 shows the flowchart of the proposed method. As this figure shows, our method consists of three parts:

- Level set initialization by user
- SVM training and testing process
- Automatic segmentation by level set evolution

In the segmentation framework, the user only needs to input the samples of tumor region into SVM training process, in the level set initialization phase. After that,

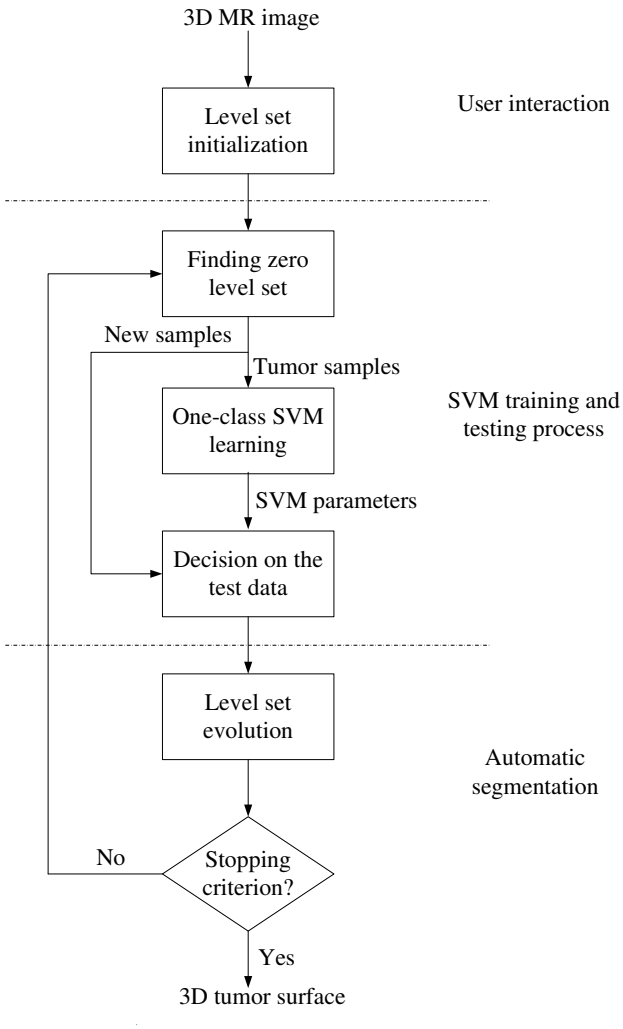

Figure 4.3: The schematic diagram of the SVM-based segmentation method.

the algorithm iterates between SVM process and level set evolution. In other words, using the tumor samples inside the zero level set, SVM can learn the data distribution, map the data to a higher dimensional space, and optimally turn out a separating plane for it. Then, this trained SVM is used to test the new samples that the level set intends to accept. By growing the level set, the number of training

set enlarges that causes the more accurate tumor distribution learning by SVM. This iterative process continues until the level set reaches to the tumor boundary and the stopping criterion is met. In the following sections, these three parts of the algorithm are discussed in detail.

4.2.1 SVM process

As described earlier, in our method SVM is used iteratively in order for guiding level set to grow properly. Using an initialized tumor set, the optimal values of the SVM parameters are obtained and then these trained SVM is used to test the new samples and defined the level set speed function. This process continues in each iteration of level set growing until there are no samples that are decided as tumor by SVM. Therefore, the accuracy of the segmentation is highly dependent on the generalization ability of SVM, i.e., how well it can decide on the new samples using the training set.

The generalization ability is influenced by several factors, the most important of which is the accuracy of the training set. Moreover, the algorithm is used for tumor segmentation in the MR images and in most of the cases, MR images are noisy. Therefore, the training set may contain some noise intensities that decrease the accuracy of the training set and thereby affecting the performance of the testing process. To remedy this problem, the concept of confidence interval is used.

Based on the definition of confidence interval and confidence level in Sec. 3.2.1, the problem can be solved if we use a confidence interval of the training samples for SVM learning process. Such an interval can provide us with a level of confidence about the training set and remove the noise intensities from this set. Since the mean intensity of tumor region is assumed to be grater than that of the non-tumor region, as it is mentioned in the previous chapter, the one-tailed confidence interval is applied in this approach. Let $\chi_i = \{I_{ij}(x, y, z) = x_{ij}\}_{j=1}^{n}$ denote the intensities of accepted tumor samples up to the ith iteration. The new training set can be defined as

$$\chi_i' = \{x_{ij} \geq (\hat{\mu}_i - k\hat{\sigma}_i)\} \qquad i \geq 0 \tag{4.16}$$

where $\hat{\mu}_i$ and $\hat{\sigma}_i$ are the sample mean and standard deviation of χ_i, respectively, and are calculated as (3.15).

The SVM learning process is performed on the new training set and the training parameters are obtained. The decision function of the $(i+1)$th iteration is defined based on the calculated support vectors $\{\alpha_{ij}\}$, bias value b_i, and also the RBF kernel function.

$$\begin{aligned} \text{Train SVM} \quad & (\chi_i', \upsilon, \sigma_i^2) \rightarrow (\{\alpha_{ij}\}, b_i) \\ f_{i+1}(x) \quad &= \quad \text{sgn}\left(\sum_{x_{ij} \in \chi_i'} \alpha_{ij} K(x_{ij}, x) - b_i\right) \end{aligned} \tag{4.17}$$

The parameters υ and σ_0^2 in the SVM training process must be defined by user. We set $\upsilon = 0.05$ that let SVM consider high fraction of training data set in the learning step. Moreover, we select $\sigma_0^2 = 0.5$ and $\{\sigma_i^2\}$'s for the other iterations are defined using (4.15).

4.2.2 Level set speed function design

In the proposed approach, the level set method is applied to extract the 3D tumor surface using the samples that are classified by SVM. Therefore, the speed function of the level set, which is one of the main challenges of such algorithms, must be defined properly. Since the level set evolves on the SVM classified samples, the output of the SVM decision function can be used as an image-based factor in the speed function definition. Thus, the level set speed function in (x, y, z) image space and in the jth iteration is defined as

$$F^{(j)}(x, y, z) = F_0.f_j(I(x, y, z)) - \epsilon\kappa_\phi \qquad j \geq 1 \tag{4.18}$$

where F_0 is a constant propagation determined by a positive number and $f_j(I(x, y, z))$ is the output of the SVM decision function for the image sample in (x, y, z) dimension and with the intensity of $I(x, y, z)$.

It should be noted that the sign of f_j indicates whether the sample is inside (+) or outside (-) the tumor region. Therefore, when $f_j = +1$, the level set grows

with the positive speed of $F^{(j)}$ and when $f_j = -1$, the level set shrinks with the negative speed of $F^{(j)}$. This parameter in the speed function is the image-based term and causes the level set to finally be attracted to the tumor boundary.

4.2.3 Level set initialization

The level set initialization in this approach is the same as the initialization step in the TLS approach. In this algorithm the level set is also initialized inside the tumor region since the initial SVM training process is performed using this initial set. Moreover, depending on the complexity of the tumor shape and convexity or concavity of it, some small spheres are inserted inside the tumor region in the reference slice as the initial zero level set. Parameter f_1 is calculated by (4.17) only based on the selected tumor samples in the reference slice. Since the initialization process is as described in Sec. 3.2.4, we do not discuss it again.

4.2.4 Stopping criterion

As described, our method updates the SVM training parameters iteratively using accepted tumor samples up to the each iteration. The level set speed function is also updated at each iteration based on the SVM decision function. At the tumor boundary, the negative level set speed for non-tumor samples causes the level set to reject them. Therefore, the rate of accepting new samples declines so that the

variations of the zero level set volume becomes negligible per iteration. This fact helps us to define the stopping criterion.

The algorithm will stop when for t_s consecutive iterations the ratio of the new accepted voxels to the total number of voxels inside the zero level set goes below a threshold value, ε. The choice of ε express a trade-off between the accuracy of the segmentation and the speed of the convergence. It is empirically determined and in our algorithm, we set $\varepsilon = 10^{-4}$ as the threshold value. However, for the large enough values of t_s and a small value of ε, the overall performance of the algorithm is not affected significantly by the values of these parameters.

4.2.5 Narrow band solutions

For a two-dimensional (2D) interface evolving in three dimensional (3D) space, the level set algorithm is at least an $O(N^3)$ method per time step, where N is the number of points in the spatial direction. One drawback of this technique stems from the computational expense, since by embedding the interface as the zero level-set of a higher dimensional function, a 2D interface problem has been transformed into a 3D problem (Fig. 4.4). Clearly, the disadvantage of heavy computational load is even worse for a 3D level set approach.

In order to overcome this drawback, Adalsteinsson and Sethian proposed a fast level set method for propagating interfaces, called the narrow band method [47].

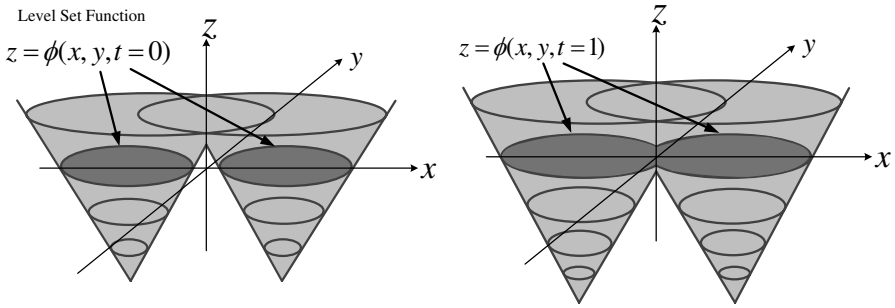

Figure 4.4: An extra dimension added in solving the front propagation problem.

The main idea of the narrow band is to modify the level set method so that it only affects points close to the region of interest, namely the cells where the front is located. We have applied this method to our proposed approaches and in this section, we describe it in detail.

In Fig. 4.5, the bold curve depicts the level set and the shaded region around it is the narrow band. The narrow band is bounded on either side by two curves (in 2D) or surfaces (in 3D) that are a distance d apart. The value of d determines the number of grid points that fall within the narrow band. During a given time step, the value of ψ outside the narrow band is stationary and the propagating front cannot move past the narrow band. As a consequence of this updating strategy, the front can be moved through a maximum distance of d, either inward or outward, at which point we must rebuild an appropriate (a new) narrow band. We reinitialize the level set function by treating the current zero level set configuration, i.e. $\psi = 0$, as the initial hypersurface $\gamma(0)$. This technique reduces the computation time

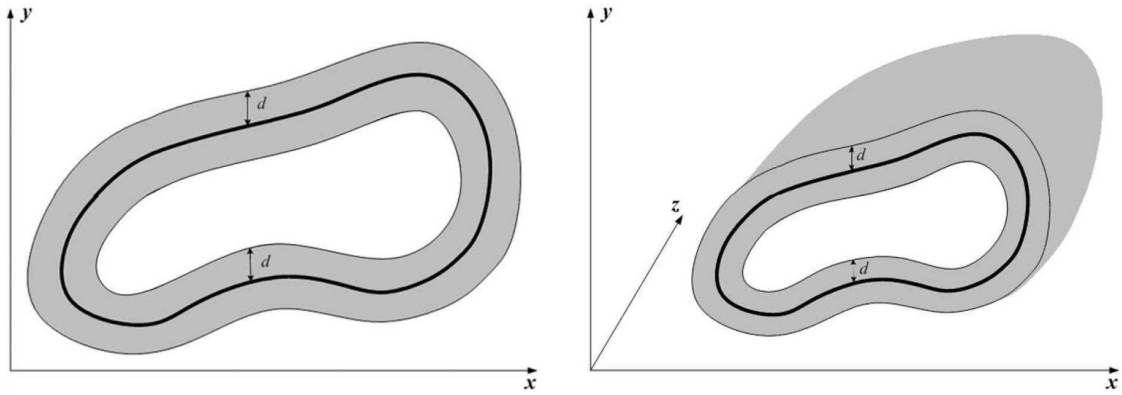

(a) (b)

Figure 4.5: Narrow band illustration. (a) 2D narrow band, (b) 3D narrow band.

significantly when compared with the full sized method, especially for 3D level set based approaches.

The narrow band method relies on the fact that when solving for only a single level-set, $\psi(p,t) = 0$ (p is the point on the front), the evolution of ψ is important only in the vicinity of that level-set and the evolution equations for ψ are such that the level sets of ψ evolve independently (to within the error introduced by the discrete grid). Thus, one should perform calculations for the evolution of ψ only in a neighborhood of the set $S = \{p|\psi(p) = 0\}$ and the rest can be ignored.

However, the narrow band rebuilding and ψ reinitializing during the front propagation are not trivial. The challenge is how to keep track of the neighbors, as the zero level set of ψ moves from one set of voxels to another. We can adopt two schemes for constructing the narrow band. Since the reinitialization process is the most time consuming step of the narrow band method, in the first scheme we try

to reduce the need to this process.

In the first scheme, a manually drawn volume of interest is considered around the tumor region and the entire process in performed inside it. In this scheme, a wide narrow band is built around the zero level set. While the front lies in the narrow band, only the grid points inside the band are updated in each time step, and when it reaches the narrow band boundary, the level set function is reinitialized on the whole grid points and the new narrow band is built. By this way, in each time step the updating process is done for the limited set of the grid points and after some time steps, a reinitialization process is done for all grid points.

This approach can reduce the computational expense of the algorithm, especially for the small object of interest. For the large objects, however, the algorithm is still computationally expensive. The reason is because in such cases the volume

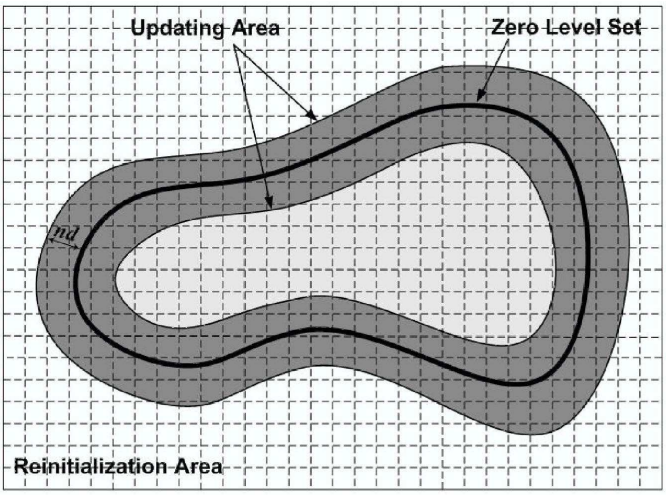

Figure 4.6: 2D projection of a two-layer narrow band construction.

of interest is large and therefore, the number of grid points that must be considered in the level set reinitialization are also large. Moreover, there is a limitation in the width of the narrow band so that a very wide band makes the algorithm unstable. The 2D projection of this structure, that is called 2-layer NB, is shown in Fig. 4.6.

In the second scheme, we build a four-layer narrow band to implement the level set method. Therefore, we call it 4-layer NB and its 2D projection is shown in Fig. 4.7. The first layer (dark gray) contains the set of grid points that lie adjacent to the zero level set and in its immediate neighborhoods. These immediate neighbors construct the actual boundaries of the narrow band. The second layer (light gray) contains the grid points in the next neighborhoods of the zero level set that are used to compute the second order derivatives of ψ for calculating the mean curvature κ. These next neighbors construct the boundary of the reinitialization

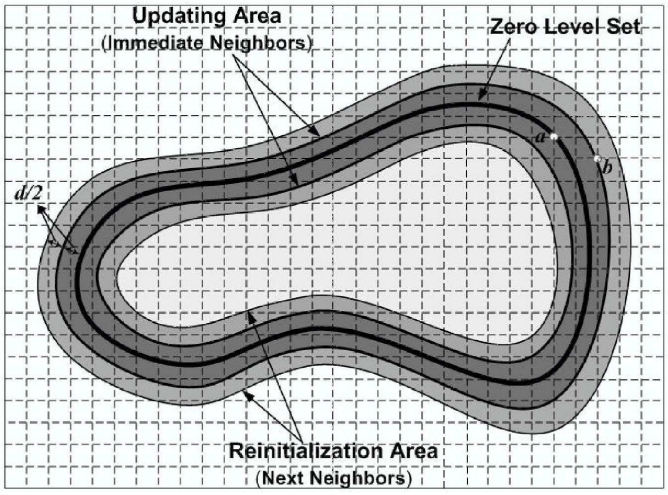

Figure 4.7: 2D projection of a four-layer narrow band construction.

build a four-layer narrow band around the current front.
for every point a on the current front
  update $\psi(a)$.
  if $\psi(a)$ is grater than $d/2$
    surface expands and then add the immediate outside neighbor b to the adjacent set.
    remove a from the adjacent set and set it as the inside neighbor.
  else if $\psi(a)$ is less than $-d/2$
    surface shrinks and then add the nearest inside neighbor b to the adjacent set.
    remove a from the adjacent set and set it as the outside neighbor.
  endif
endfor
reinitialize ψ for all points in the reinitialization area.

Figure 4.8: Strategy for rebuilding the narrow band and reinitializing the level set function at each time step using 4-layer NB.

area. When the surface evolves, we need to update the value of the level set function ψ at each point which is initially on the zero level-set, as well as the narrow band. The strategy for rebuilding the narrow band and reinitializing ψ at each time step is shown in Fig. 4.8.

Using this scheme, the updating and reinitializing processes are performed at each time step and for a limited set of the grid points. Therefore, this scheme removes the necessity of drawing a volume of interest and thereby reducing the user involvement. Moreover, it can reduce the computational expense of the algorithm even for large objects.

There is a trade-off between the complexity of the narrow band scheme and the computational time of the level set algorithm. For the small objects, the 2-layer NB scheme is more effective and provides sufficient reduction in the computational

time. However, for the large objects, the computational time reduction due to the 4-layer NB scheme can compensate for the complexity of its implementation.

4.2.6 A faster algorithm

The narrow band solution improves the speed of the algorithm dramatically when compared with the full size method. However, the computational time increases rapidly with the number of grid points that reside in the narrow band, since the narrow band rebuilding and level set reinitializing at each iteration take up most of the processing time. For example, in the case of Tumor 13, every run of the algorithm to completely detect the 3D tumor surface takes around 40 minutes with the 4-layer NB scheme (note that the algorithm is programmed using Matlab and runs on a PC with 3.0GH CPU and 512MB memory). This obviously restrains its practical use in clinical activities.

One way to speed up the algorithm further is to reduce the number of voxels in the narrow band or the number of iterations or both of them. In this work, the narrow band size is reduced simply by compressing the original image into 1/4 of it, that is, rearranging the image data by sampling them along x and y directions, respectively. We do not sample the image along the z axis, since the resolution of MR images in this direction is not very high. Figure 4.9 illustrates the data sampling mechanism.

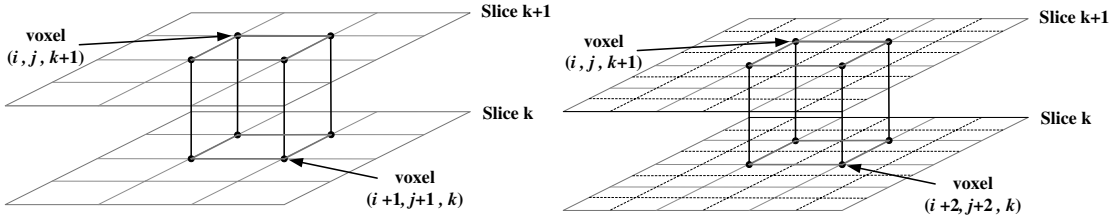

Figure 4.9: Illustration of image sampling, (a) voxels concerned with the computation in the original image, (b) image data sampling along x and y directions.

After image size reduction, we apply the level set algorithm with the narrow band solution. By this way, the voxels concerned with the computation, are reduced significantly. Moreover, the iteration number for deforming the evolving front to the desired tumor surface is also reduced, accordingly. As expected, this fast algorithm of level set method reduces the computational time to at least 1/4 of that needed by the narrow band solution alone. The run time of each algorithm is summarized in Table 4.1.

To measure the effects of such reduction, in image size, on the accuracy of the segmentation, two sets of results obtained by the 4-layer narrow band scheme and its faster algorithm are compared with the references, respectively, using a validation method presented in Chapter 5. The results of comparison are shown in Fig. 4.10. This figure clearly shows that there are no significant differences in accuracy between the narrow band solution and the faster algorithm. However, if we increase the image size reduction ratio, for instance 1:3 , the accuracy of the results will no longer be guaranteed.

Table 4.1: Comparison of the run time between narrow band solutions and the faster algorithm

Tumor	**Volume** (mm^3)	**Run Time**			
		narrow band solution		fast algorithm	
		2-layer	4-layer	2-layer	4-layer
2	18252	50′04″	36′25″	11′46″	08′02″
3	13771	46′30″	28′04″	07′13″	05′07″
6	6600	20′03″	13′15″	04′02″	03′10”
8	7556	16′12″	10′35″	02′11″	01′52″
11	13512	08′31″	05′24″	01′34″	00′40″
13	50808	58′54″	37′23″	12′35″	08′57″
16	16485	12′47″	07′50″	02′16″	01′30″

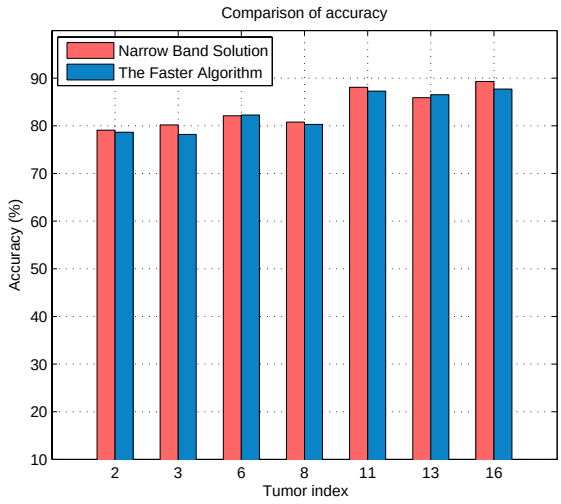

Figure 4.10: Accuracy comparison between 4-layer narrow band scheme and its faster algorithm.

4.3 Test results and discussion

We apply this algorithm to our dataset to test its performance. In our tests, the value of k is set to $k = 2$. This value of k provides us with a reasonable confidence

interval which contains more than 80% of the training samples. Figure 4.11 shows the final segmentation results by this approach on the same tumors that were used in the previous chapter. However, different image slices are shown in this figure. Similar Fig. 3.22, the 3D tumor shapes are shown in the right-most column, and the cross-sections of the extracted tumor surfaces with the slices are shown in the other columns. The subjective comparison between the segmentation results and their ground truths indicates a good agreement between them. Moreover, the subjective comparison between the segmentation results of two proposed approaches in Chapters 3 and 4 indicates the TLS superior performance. The objective evaluation of this method and the quantitative comparison between these two approaches are provided in Chapter 5.

This figure also show that the proposed method can segment the tumors with non-homogeneous intensities. The reason is because SVM is only trained using the samples inside the confidence interval and not all the samples inside the zero level set. Therefore, if there is a non-homogeneity inside the tumor region, the smoothness parameter in the level set speed function causes the level set to accept those samples, while they are not considered in the SVM learning process.

4.4 Summary

This chapter presents a novel one-class SVM-based approach for 3D tumor segmentation in the brain MR images. This method also uses the level set as a deformable model and defines its speed function on the basis of one-class SVM training and testing process. Therefore, as in TLS approach, no explicit knowledge about the density functions of the tumor and non-tumor regions are required. Moreover, using one-class SVM leads the user interaction to be reduced to a simple level set initialization and removes the time consuming non-tumor sampling. In order to train the SVM, samples inside the zero level set are used and the training is iteratively refined as the level set grows. The visualization evaluation of the segmentation results demonstrates that our method can effectively segment both concave and convex tumors. However, this subjective evaluation shows that the results for convex bodies have higher precision than the results for concave ones. Furthermore, this method can also segment the tumors with non-homogeneous intensities. The proposed method is suitable not only for tumor segmentation, but also for other tissue segmentation or extraction. It can also be applied in 2D space to extract the contour of the desired regions.

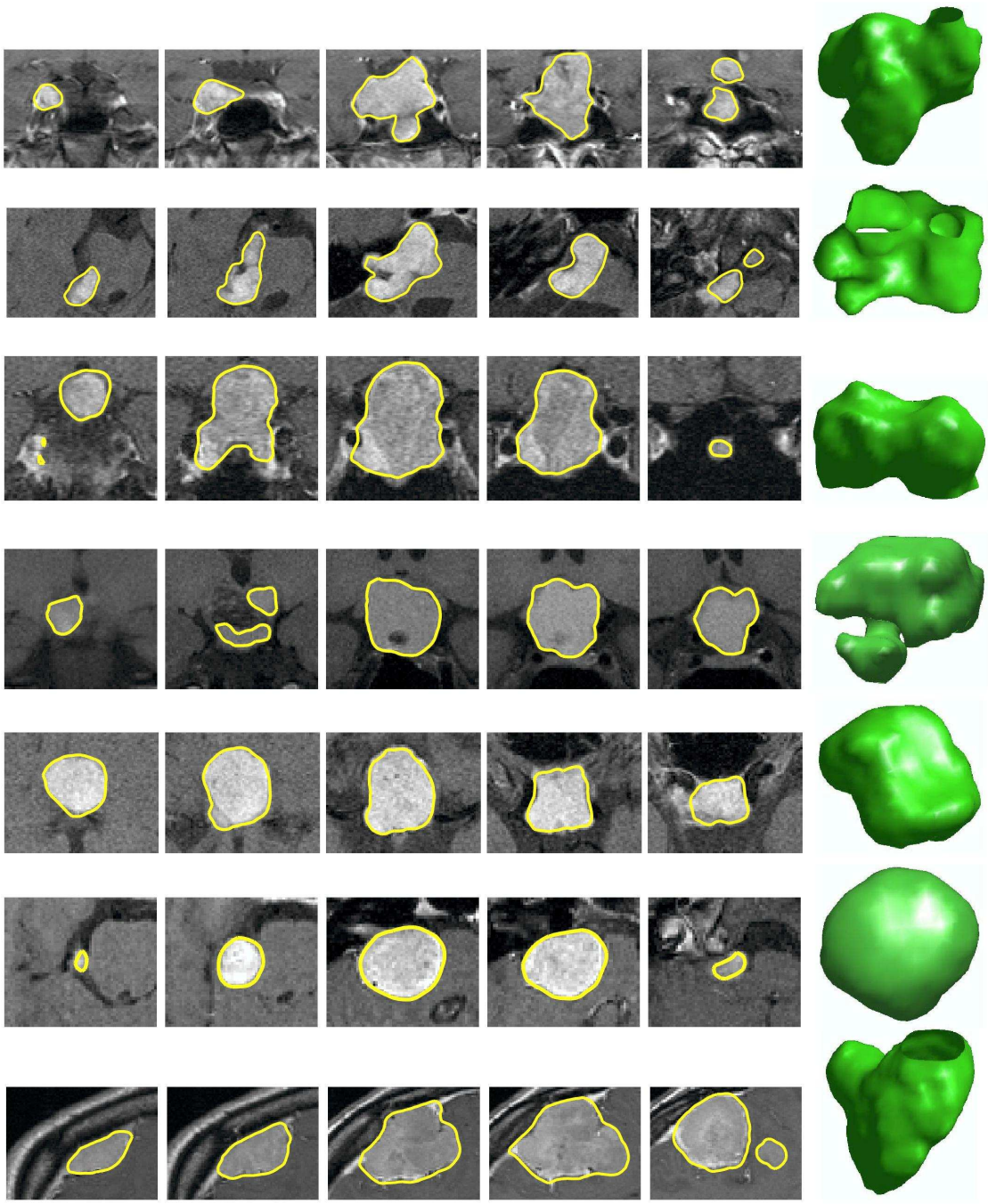

Figure 4.11: The final segmentation results using SVM-based approach. The indexes of tumors from top to bottom are: 2, 3, 5, 6, 8, 11 , and 13. First five columns are some cross-sectional images of the 3-D tumors in the last column.

Chapter 5

Results and Discussion

The validity of the segmentation results are very important, especially for medical images. The reason is because any significant disagreement between the detected results and the real targets might lead to severe damages in clinical activities. Therefore, it is very important to evaluate the performance of the algorithm before the results are used in clinical decision for the diagnosis and treatment of the tumors. This chapter discusses the evaluation criteria and provides algorithm verification based on the experimental results. Comparisons between the performances of the proposed methods are provided. The segmentation results are also compared with the results of an existing region-competition based segmentation algorithm.

5.1 Validity evaluation

Validity refers to the degree of accuracy for the specific concept that the researcher is attempting to measure. To evaluate the validity of an algorithm, usually comparison of a new measure against an existing gold standard is conducted. The accuracy of computer-assisted segmentation of medical images is difficult to quantify in the absence of a ground truth. Traditionally, there are two mechanisms for validation, if no ground truth data are provided [5]:

- Create synthetic images with known size and shapes, segment them with the proposed method, and contrast the values to those used when generating the image.

- Train some human operators to segment a set of defined volumes (most of the time it is necessary to repeat the segmentation in order to evaluate their variability), then compare the segmentations results using proposed method with their manual segmentations.

Although physical or digital phantoms can provide a level of ground truth, they have been unable to reproduce the full range of imaging characteristics such as partial volume artifact, intensity inhomogeneity, and the normal and abnormal anatomical variability observed in the clinical data. Therefore, interactive drawing of the desired segmentation by experts has often been the only acceptable approach.

5.1.1 Validation metrics

Measuring the performance of algorithms for image segmentation requires an appropriate metric, a goodness index, that gives us a valid measure of the quality of the segmentation result. Various validation methods have been proposed in the literature [48, 49, 50, 51]. A good source and discussion of such techniques can be found in [52]. Typical procedures for validation of computer-assisted segmentation are also listed in [53, 54]. However, the most appropriate way to carry out the comparison of an automated segmentation to a group of expert segmentations is still unclear [51]. In the following, some metrics that can be used for the validation of segmentation algorithms, are listed.

Volumes

A feature that is easily accessible for evaluation is the total volume of a structure. This is the simplest morphologic measure and often used in reliability studies in neuroimaging applications [54]. For binary segmentations, the number of voxels in the volume is calculated. However, a more precise volumetric measurement is possible by fitting a surface (e.g., marching cubes) with sub-voxel accuracy and calculating the volume by integration. Comparing volumes of segmented structures does not take into account any regional differences and does not give the locations of differences. Furthermore, such comparison cancels the over and un-

derestimation along boundaries or surfaces and may give excellent agreement even if the segmentation result is poor.

Volume Overlap

This metric is the pair-wise comparison of two binary segmentations by relative overlap so that it takes into account the spatial properties of structures. Assuming spatial registration, images are analyzed voxel by voxel to calculate false positive (FP), false negative (FN), and true positive voxels (TP). Let Ω_G and Ω_S denote the set of tumor voxels in the ground truth and the corresponding set resulting from segmentation algorithm, respectively. The values of true positives, false positives, and false negatives are defined as follows. These values are also shown in Fig. 5.1.

$$\begin{aligned} \text{TP} &= \{x(i,j,k) | x \in \Omega_G, x \in \Omega_S\} = \Omega_G \cap \Omega_S \\ \text{FP} &= \{x(i,j,k) | x \notin \Omega_G, x \in \Omega_S\} = \overline{\Omega_G} \cap \Omega_S \\ \text{FN} &= \{x(i,j,k) | x \in \Omega_G, x \notin \Omega_S\} = \Omega_G \cap \overline{\Omega_S} \end{aligned} \tag{5.1}$$

where $x(i,j,k)$ represents the intensity of image voxel at the (i,j,k) location.

Well accepted measures are the intersection of Ω_G and Ω_S divided by their union, known as Jaccard's measure (JM), $\text{JM} = \#(\Omega_G \cap \Omega_S)/\#(\Omega_G \cup \Omega_S)$, or intersection divided by reference, called percentage match (PM), $\text{PM} = \#(\Omega_G \cap \Omega_S)/\#\Omega_G$. Both measures give a score of "1" for perfect agreement and "0" for

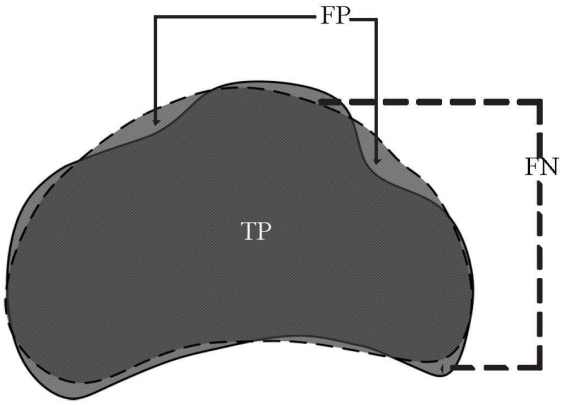

Figure 5.1: Three different areas defined by the two corresponding outlines, true positive (TP), false positive (FP), and false negative (FN).

complete disagreement. However, the first measure, JM, is more sensitive to the differences between two sets, since both denominator and numerator change with increasing or decreasing overlap. The overlap measure depends on the size and the shape complexity of the object. Assuming that most of the error occurs at the boundary of objects, small objects are penalized and get a much lower score than large objects.

Probabilistic distances between segmentations

In most medical image segmentation tasks, there is no clear boundary between anatomical structures so that absolute ground truth by manual segmentation does not exist and only a fuzzy probabilistic segmentation is possible. In such cases, manual probabilistic segmentations is generated by aggregating repeated multiple segmentations of the same structure. Therefore, a probabilistic overlap measure is

derived between two fuzzy segmentations based on the normalized distance between two probability distributions as follows:

$$\mathrm{POV}(A,B) = 1 - \frac{\int |P_A - P_B|}{2\int P_{AB}} \tag{5.2}$$

where P_A and P_B are the probability distributions representing the two fuzzy segmentations and P_{AB} is their joint probability distribution.

Hausdorff distance

The Hausdorff-Chebyshev metric defines the largest difference between two contours/surfaces. Given two surfaces S and S', for each point p on S the minimal distance to all the points on surface S' is calculated as

$$d_S(p,S') = \min\{d_{pp'}(p,p') = \| p - p' \|_3,\ p' \in S'\} \tag{5.3}$$

where $\| \cdot \|_3$ denotes the usual Euclidean norm in 3D space. This minimal distance is calculated for each surface point and then, the maximum minimal distance is calculated as the worst case distance, $h_S(S,S') = \max\{d_S(p,S'), p \in S\}$. The Hausdorff metric is not symmetric so that $h_S(S,S')$ is not equal to $h_{S'}(S',S)$. However, we define a symmetrical Hausdorff distance (HD) metric by maximizing over two one-sided errors:

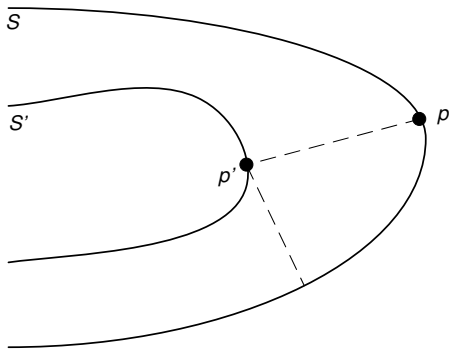

Figure 5.2: One-sided error. In this case, $h_S(S, S')$ is longer than $h_{S'}(S', S)$, since $d_S(p, S') > d_{S'}(p', S)$. Thus, a small one-sided distance does not imply a small distortion.

$$\mathrm{HD}(S, S') = \max\{h_S(S, S'), h_{S'}(S', S)\} \tag{5.4}$$

Such a symmetrical distance can provide a more accurate measurement of the difference between two surfaces, since the one-sided error can lead to underestimated distance values, as illustrated in Fig. 5.2.

The Hausdorff distance metric calculation is computationally expensive, as we need to compare each surface point with all the other points. A comparison of complex 3D surfaces would require a huge number of calculations. This measure is extremely sensitive to outliers and may not reflect the overall degree of matching.

Mean absolute surface distance

The mean absolute surface distance tells us how much on average the two surfaces differ. We can define the mean distance between two surfaces S and S' having the

point-to-surface distance defined in Eq. 5.3:

$$d_m(S, S') = \frac{1}{|S|} \int \int_{p \in S} d(p, S') dS \tag{5.5}$$

where $|S|$ denotes the area of S. This calculation is also not symmetric. We, therefore, derive a common average by combining the two averages and define a symmetrical version of the mean error as the mean absolute surface distance (MASD):

$$\text{MASD}(S, S') = \max\{d_m(S, S'), d_m(S', S)\} \tag{5.6}$$

The mean absolute surface distance does not depend on the object size.

5.2 Segmentation validation

To validate our algorithms, three validation metrics are used in this thesis, which are Jaccard's measure (JM) or volume overlap metric, Hausdorff distance (HD), and mean absolute surface distance (MASD).

5.2.1 TLS segmentation validation

The quantitative validation of the TLS segmentation method is presented in Table 5.1, which also shows the volumes of the segmented tumors. The results for the surface distance metrics (HD and MASD) indicate that the segmentation is

reliable. The values of these metrics for various tumors are more similar compared to JM. The variable JM values demonstrate that this metric is more sensitive to the size and complexity of tumors. It should be noted that the large values of HD in some cases is due to the presence of outliers.

Table 5.1: Quantitative validation of TLS segmentation results

Index	**Volume**(mm^3)			**Overlap** (JM%)		**Hausdorff**(mm)		**MASD** (mm)	
	GT	Search	Adaptive	Search	Adaptive	Search	Adaptive	Search	Adaptive
1	12454	9220	10331	72.8	78	4.895	4.668	0.936	0.795
2	18252	16170	16676	80.5	83	10.32	9.12	1.15	0.96
3	13771	11313	12654	79.8	84.5	5.615	5.63	0.679	0.72
4	10619	8508	9655	75	84	3.941	3.938	0.75	0.756
5	14147	13818	14118	79.8	84.1	5.127	4.311	0.831	0.793
6	6600	5933	6280	80.7	88.5	1.771	2.013	0.553	0.576
7	28328	26013	27589	87	89	4.196	4.693	0.788	0.875
8	7556	7056	7538	83	87	11.5	11.34	0.91	0.895
9	15858	14424	16899	90.6	87.4	9.44	8.28	0.756	1.104
10	6944	6503	6362	89.6	88	10.78	10.8	0.804	0.802
11	13512	12928	12528	91.8	90.6	2.502	2.168	0.724	0.656
12	21227	22068	20033	86.4	90.6	6.174	7.332	0.952	0.76
13	50808	49008	48648	88.5	90.1	6.848	6.38	0.864	0.814
14	17793	16582	17434	92.9	93	6.076	2.246	0.637	0.642
15	14159	14153	14300	90.6	91	3.82	3.514	0.823	0.8
16	16485	14735	15882	88.5	91	5.19	3.95	0.667	0.646

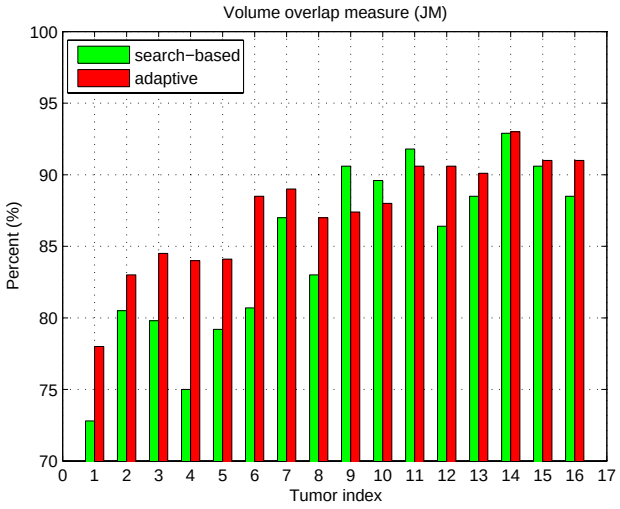

Figure 5.3: Comparison between search-based and adaptive schemes in term of volume overlap metric (JM).

Figure 5.3 compares JM for the two TLS schemes. As we can see in this figure and also in Table 5.1, the variation of JM in the search-based scheme is from 72.8% to 92.9% with a mean of $84.8 \pm 6.2\%$, and in the adaptive scheme from 78% to 93% with a mean of $87.5 \pm 3.9\%$. Thus, the adaptive scheme generally performs better than the search-based scheme.

The first six tumors, as mentioned, have concave bodies while the other tumors are convex. We see in Fig. 5.3 that the segmentation error for concave tumors is generally higher than that for convex ones. This observation can be justified by the complexity of the tumor shapes and the effect of the smoothness parameter on the level set speed function. Moreover, since the initial level set has a convex shape, it grows more perfectly in a convex tumor than a concave one.

In the case of concave tumors, adaptive TLS gives better results, while for convex tumors, it is possible that search-based TLS performs better. In fact, the adaptive algorithm helps the level set to grow inside the complex parts of the tumor. Therefore, for concave tumors search-based TLS cannot be as good as adaptive TLS, however, for convex tumors (especially those with a very simple shapes) exhaustive search can find a proper value for k so that the segmentation results become better than results using the adaptive scheme. In the cases of Tumors 11, 14 and 15, the performance of both search-based and adaptive TLS are almost the same. Considering their respective images, the reason is because the intensity overlap between the tumor and non-tumor regions in these cases are relatively small.

The maximum values of JM in both search-based and adaptive schemes occur for Tumor 14 while the minimum JM in both cases occur for Tumor 1. Considering their respective tumor shapes, we realize that Tumor 14 is among the tumors with the simplest shape and the most contrast between tumor and non-tumor intensities. Tumor 1 is among those with the most complex shape and the least contrast between tumor and non-tumor intensities. This also verifies the higher performance of TLS for simple and convex tumor shapes with higher intensity difference between the tumor and its surrounding tissues.

5.2.2 SVM-based segmentation validation

The results of SVM-based segmentation method are also quantitatively evaluated using validation metrics. Table 5.2 shows the validation results for 13 MR images. As can be seen in this table, the variation of the JM is from 78.2% to 89.97% with a mean of $84.68 \pm 4.1\%$. Moreover, the values of the surface distance metrics (HD and MASD) in this table show that there are not large distances (maximum

Table 5.2: Quantitative validation of SVM-based segmentation results

Index	**Volume**(mm^3)		**Overlap**(JM%)	**Hausdorff**(mm)	**MASD** (mm)
	GT	SVM			
2	18252	15323	78.66	12.91	1.308
3	13771	11854	78.2	9.516	1.172
5	14147	12724	81.93	8.574	1.43
6	6600	5998	82.27	2.895	0.574
7	28328	22124	83.86	5.22	0.97
8	7556	6597	80.3	9.223	0.953
9	15858	15012	89.5	8.873	0.744
10	6944	6027	85.69	12.32	0.798
11	13512	11400	87.3	2.147	0.610
13	50808	49068	86.53	8.49	0.98
14	17793	16288	89.97	7.10	0.646
15	14159	14377	88.98	6.66	0.986
16	16485	15217	87.72	7.45	0.801

and absolute) between the segmented and the corresponding reference surfaces. This indicates the reliability of the SVM-based approach. In this table, the first 4 tumors are concave and the other tumors are all convex.

As the table shows, the segmentation error for concave tumors is almost higher than that for convex tumors, which is consistent with the TLS results. Moreover, similar to the TLS results, the maximum value of JM occurs for Tumor 14 and its minimum is for Tumor 3 (we did not apply this algorithm to Tumor 1, 4, and 12). Tumor 3 also has a complex shape and low contrast between tumor and non-tumor intensities.

Table 5.3 shows the values of FP and FN resulted from evaluation of the SVM-based approach. As can be seen, the values of FP in the segmentation results are lower than the values of FN. It is due to the characteristic of one-class SVM which tries to learn the non-linear tumor distribution only using the samples from tumor region and without any knowledge about non-tumor region. Therefore, in the testing process, the samples are accepted as the tumor class which are more similar to the training set compared to the other samples. Consequently, the

Table 5.3: The values of FP and FN resulted from the SVM-based approach.

Index	2	3	5	6	7	8	9	10	11	13	14	15	16
FP (# of voxels)	92	104	106	22	22	50	71	7	3	88	25	70	67
FN (# of voxels)	590	431	348	158	821	213	220	163	267	173	281	123	286

number of samples which are inside Ω_G but are not accepted by the level set (FN) are more than the number of those false samples which erroneously are accepted by the level set (FP).

It should be noted that segmentation of concave tumors results in the higher values of FP and FN compared to the segmentation results of convex tumors. Because of the complexity of concave tumor shape as well as the effect of smoothness parameter on the level set speed function, the segmentation process results in the smaller number of TP while larger number of FP compared to those of convex tumors, thus, the error of segmentation for these concave tumors is higher.

5.3 Comparison between TLS and SVM-based approaches

In this section, we compare the performances of TLS and SVM-based approaches based on the values of evaluation metrics. Moreover, the comparison between the convergence rates of these two approaches is provided. Figure 5.4 compares three evaluation metrics among both schemes of TLS and the SVM-based approach. As Fig. 5.4(a) shows, the values of volume overlap measure (JM) for the SVM-based method are generally lower than the corresponding values for adaptive TLS. Moreover, the comparison between these values for SVM-based and search-based

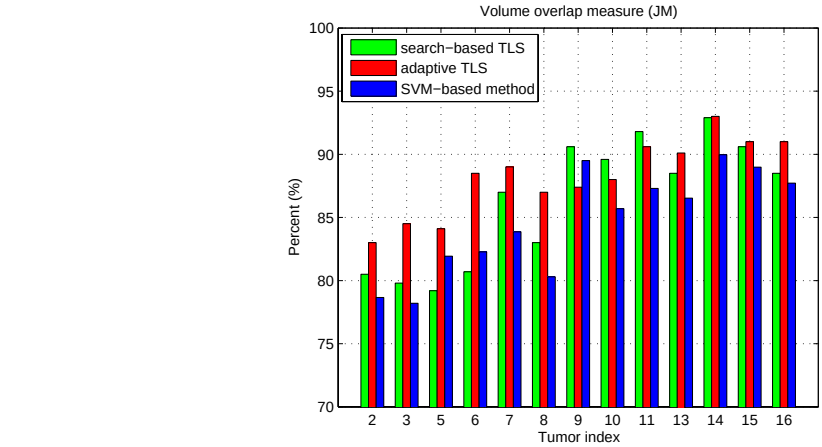

(a) Volume overlap (JM)

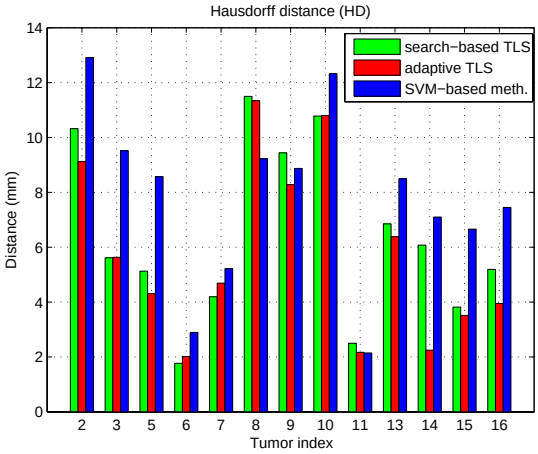

(b) Hausdorff distance (HD)

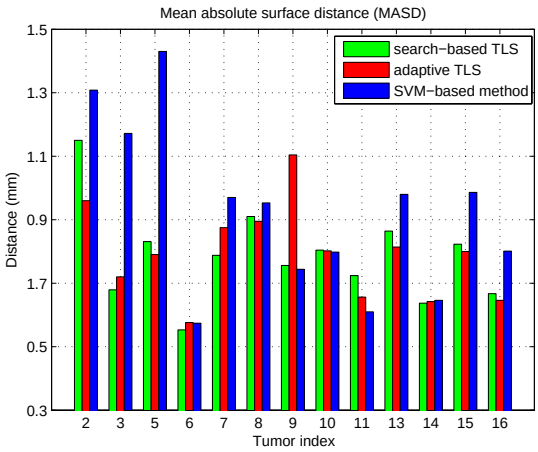

(c) Absolute distance (MASD)

Figure 5.4: Quantitative comparison between TLS and SVM-based approaches.

schemes indicates that on average these two schemes perform the same. These observations are also verified by the values of min, max and mean of JM provided in the previous section. Based on those values, the average of JM for SVM-based and search-based TLS schemes are similar and both of them are lower than that of the adaptive TLS.

For concave tumors (first 4 tumors), JM values for SVM-based method is near

to the JM values for searched-based TLS and both of them are lower than the JM values for adaptive TLS. However, for convex tumors (last 9 tumors), these values for TLS schemes are higher than those for the SVM-based approach. Based on this observation we can conclude that, considering both concave and convex tumors, adaptive TLS is superior to the SVM-based approach. Moreover, the performance of SVM-based approach and search-based TLS for concave tumors is almost the same; however for convex tumors, search-based TLS is superior to the SVM-based approach. Such conclusions are also verified by two other figures.

Figure 5.4(b,c) show that the values of surface distance metrics (HD, MASD) for SVM-based approach are much highet than those for both TLS schemes. This also indicates that SVM-based approach does not perform well for complex and concave tumor shapes. However, for some simple tumor shapes such as Tumor 10 and 11, the values of all metrics for three schemes are similar. Especially for Tumor 11, SVM-based method performs well. This tumor, as mentioned before, has a very simple shape and good contrast between tumor and non-tumor intensities. Therefore, segmentation of simple and convex tumors using SVM-based method leads to almost the same results as the TLS schemes; however, for concave and complex tumor shapes, adaptive TLS is superior.

Convergence rate is an important factor in all the segmentation algorithm. Therefore, it is necessary to compare our proposed approaches based on this factor. For this purpose, we record the number of iterations required for the algorithms

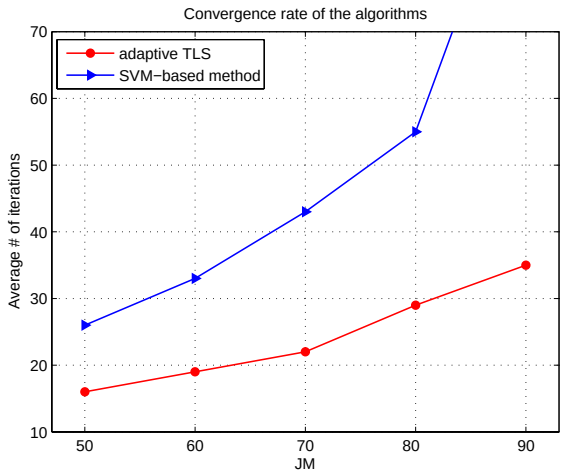

Figure 5.5: Comparison between the convergence rate of the adaptive TLS and SVM-based approaches.

to reach some JM values such as 50, 60, 70, 80 and 90% (if applicable). The iteration numbers are recorded for all the tumors and then their average for each JM value are calculated as the expected iteration number. Figure 5.5 shows the average number of iterations required for SVM-based and adaptive TLS schemes to reach the above-mentioned JM values. As can be seen, the curve corresponding to the SVM-based method is always above the other curve and also has the higher slope. This indicates that SVM-based method requires higher number of iterations to reach those JM values while adaptive TLS reaches them in the smaller number of iterations. Therefore, the convergence rate of adaptive TLS is higher than that of the SVM-based approach.

5.4 Comparison with an existing method

The segmentation results of TLS and SVM-based approaches are also compared with the results of the method proposed in [29]. As mentioned in Sec. 2.4, this method is based on region-competition and we call it the RC method. In this algorithm, the speed function is defined using the idea proposed in [29], while the other parameters in the level set equation are the same as those in the TLS and SVM-based approaches. We compare our approaches with RC for some tumors whose pre- and post-contrast T1 images are available. Figure 5.6 shows the quantitative comparison of the RC segmentation results with the results of both TLS schemes as well as the SVM-based approach for four tumors (2, 5, 8, and 11).

As seen in Fig. 5.6(a), the JM score in RC is generally less than the other approaches, but, for Tumor 11 their values are about the same. Among these approaches, the adaptive TLS gives the highest JM values except for Tumor 11, where search-based TLS performs the best. The reason is because this tumor has a simple convex shape so that its surface can be simply extracted. Furthermore, as mentioned in [29], RC works better for simple and convex tumors than for complex and concave ones. This can also be verified in two other figures.

In Fig. 5.6(b,c), the distance metrics (HD and MASD) for convex tumors (8, 11) for RC are close to those of the TLS and SVM-based approaches. All the figures show that while adaptive TLS generally outperforms the other methods,

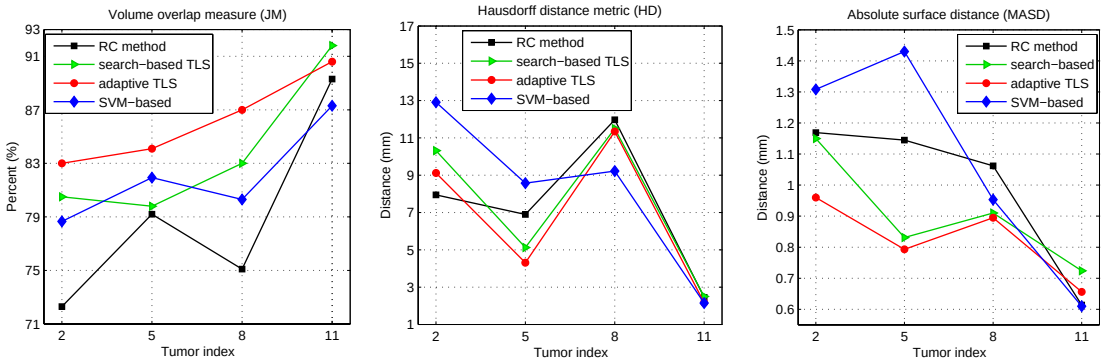

(a) Volume overlap (JM) (b) Hausdorff distance (HD) (c) Absolute distance (MASD)

Figure 5.6: Quantitative comparison of RC segmentation results with the results of adaptive and search-based TLS as well as SVM-based method using three metrics.

RC performs worse than two TLS schemes. Moreover, comparing the results of RC and SVM-based approach using Fig. 5.6 shows that for convex tumors (8, 11), SVM performs better than RC, but for concave tumors (2, 5), RC leads to the better surface distance values, however, SVM-based method gives better JM values. These results are interesting since RC uses extra knowledge (the second image) to segment the tumor while SVM-based approach and TLS, especially the search-based scheme, use no extra knowledge, however, search-based TLS may be more complex, and the adaptive TLS only takes advantage of non-tumor sampling.

5.5 Summary

This chapter evaluates the proposed approaches, TLS and SVM-based, using three evaluation metrics, volume overlap (JM), Hausdorff distance (HD), and mean ab-

solute surface distance (MASD). We compare the performance of these two approaches together and also with the performance of an existing method, called region-competition (RC) based approach. The evaluation results for each approach show that both TLS and SVM-based methods perform better for simple and convex tumor shapes than for complex and concave ones. The performances of these two approaches are higher for tumors with higher intensity differences between tumor and non-tumor regions. The comparison between two TLS schemes indicates the superior performance of adaptive TLS, however, for convex tumors search-based TLS may lead to the better results.

TLS and SVM-based approaches are compared based on the evaluation metrics and also their convergence rates. These comparisons indicate that TLS generally performs better, especially for concave tumors that the performance of SVM-based methods is not high for them. The convergence rate of TLS is also higher than that of the SVM-based method. The comparison between our approaches and the region-competition (RC) based method shows that TLS is superior to RC and SVM-based method. SVM-based method is also superior to RC for convex tumors, but for concave ones, they may perform the same. However, since RC uses the knowledge of an extra image to extract the tumor surface, both SVM-based and TLS approaches are preferred to it. Moreover, SVM-based method needs the least prior knowledge for segmentation compared to two other approaches, therefore, it is useful for simple and convex tumors.

Chapter 6

Conclusion and Future Work

6.1 Conclusion

This thesis presents two new 3D approaches based on the level set method to solve the problem of automatic (or semi-automatic with minimal user-involvement) tumor segmentation in MR images. The study of this problem is practically motivated, but has properties that make it an interesting and challenging task. Unlike the conventional deformable models for segmentation, the level set method can reduce the user intervention and be extended to 3D space without any extra machinery. The key task of the level set based method is to provide an appropriate speed function F, which can drive the evolving front to the desired surface.

Chapter 3 introduces a new threshold-based framework called TLS for 3D tumor segmentation in the brain MR images. TLS uses the level set as a deformable model

and defines its speed function based on intensity thresholding. A global threshold is defined and updated iteratively throughout the level set growing process using either a search-based or adaptive scheme. In this approach, the level set in initialized inside the tumor region and the algorithm is robust to the initialization. The TLS method can segment a variety of tumors as long as the intensity difference between tumor and non-tumor regions in each case is sufficiently large. This method does not require the information from both pre- and post-contrast MR images and only one of these image sets is sufficient. Tumors with non-homogeneous intensities can also be segmented using modified TLS, if the non-homogeneity is inside the tumor region. The visualization and subjective evaluations of the segmentation results demonstrate the effectiveness of this approach.

Chapter 4 presents another 3D tumor segmentation framework based on the one-class SVM. This method also uses the level set and defines its speed function on the basis of one-class SVM training and testing process. Using one-class SVM leads the user interaction to be reduced to a simple level set initialization and removes the time consuming non-tumor sampling required in the adaptive TLS approach. The one-class SVM is initially trained using samples inside the zero level set and then training is iteratively refined as the level set grows. The visualization evaluation of the segmentation results demonstrates that our method can effectively segment both concave and convex tumors. Furthermore, this method can also segment the tumors with non-homogeneous intensities.

Chapter 5 evaluates the performances of the proposed approaches, TLS and SVM-based, using three metrics, volume overlap (JM), Hausdorff distance (HD), and mean absolute surface distance (MASD). Moreover, it compares the performances of these two approaches together and also with the performance of an existing method, called region-competition (RC) based approach. The quantitative evaluations show that both TLS and SVM-based methods perform better for simple and convex tumor shapes than for complex and concave ones. Moreover, their performances are higher for tumors with more contrast between tumor and non-tumor intensities.

The comparison between two TLS schemes indicate the superior performance of adaptive TLS, however, for convex tumors search-based TLS may lead to better results. The comparisons among TLS, RC and SVM-based approaches indicate that TLS is superior to both RC and SVM-based methods. SVM-based method is also superior to RC for convex tumors, but, for concave ones they may perform the same. However, since RC uses the knowledge of an extra image to extract the tumor surface, both SVM-based and TLS approaches are preferred to it. Moreover, SVM-based method needs the least prior knowledge for segmentation compared to two other approaches, therefore, it is useful for simple and convex tumors.

Automatic (semi or fully) tumor surface detection methods can provide robust, consistent, and reproducible results with a certain degree of accuracy, but, such methods are still a long way from replacing the physicians. They will, how-

ever, become one of the crucial elements in the tumor treatments, particularly in computer-assisted surgery. The continued development and refinement of these methods remain as an important area of research in the future.

6.2 Future work

The proposed level set based algorithms have shown their effectiveness in 3D tumor segmentation. Sometimes these methods cannot accurately attract the evolving fronts to the desired tumor surface due to the poor contrast between the tumor and surrounding tissues, local noise, partial volume averaging, intensity inhomogeneity, and intensity non-standardization in MR images. Moreover, the image derived information based on the intensity is not enough to constrain the front propagation. The following listed future work may benefit this research.

- The acquisition of MR images is not a calibrated measure and a large variety of protocols are available for generating images with similar visual properties. This variation can cause major problems in intensity based segmentation methods, since differences in a wide variety of factors can lead to different observed intensity distributions. Therefore, we can compensate local noise, partial volume averaging, intensity inhomogeneity, and inter-slice intensity variations by preprocessing or postprocessing steps. We expect such steps to improve the overall performance of our algorithms.

- The first segmentation method presented in this thesis (TLS) determines a global threshold to segment the entire tumor. Therefore, TLS cannot segment the tumors when such a global threshold does not exist. However, this method can be extended to find several local thresholds instead of a single global one.

- Due to the poor quality of MR images, region-based methods are not accurate enough to extract tumor surface. To improve the accuracy and robustness, the information of general shape, location, and intensity distribution of the tumor could be incorporated into the models. Moreover, knowing the location of the tumor reduces the user interaction in the initialization phase and makes the algorithms completely automatic. For these purposes, digital brain atlases can be effectively used. The abnormal regions can be detected using the registered brain atlas as a model for healthy brains.

- Using both pre- and post-contrast T1 MR images or other MR modalities such as T2 in some cases may provide more helpful information and improve the segmentation results.

Bibliography

[1] S. Saini, "Radiologic measurement of tumor size in clinical trials: past, present, and future," *American Journal of Roentgenol*, vol. 176, pp. 333–334, February 2001.

[2] A. Sorensen, S. Patel, C. Harmath, and et al., "Comparison of diameter and perimeter methods for tumor volume calculation," *Journal of Clinical Oncology*, vol. 19, pp. 551–557, January 2001.

[3] M. A. Brown and R. C. Semelka, *MRI: Basic Principles and Applications*. John Wiley and Sons, Inc., 3rd ed.

[4] J. Zhou, T. Lim, V. Chong, and J. Huang, "Segmentation and visualization of nasopharyngeal carcinoma using mri," *Computers in Biology and Medicine*,

vol. 33, pp. 407–424, September 2003.

[5] S. Fan, *3D Prostate Surface Detection from Ultrasound Images*. PhD thesis, Nanyang Technological University, 2003.

[6] L. Clarke, "Mr image segmentation using mlm and artificial neural nets," *Medical Physics*, vol. 18, no. 3, p. 673, 1991.

[7] S. Vinitski, C. Gonzalez, F. Mohamed, T. Iwanaga, R. Knobler, K. Khalili, and J. Mack, "Improved intracranial lesion characterization by tissue segmentation based on a 3d feature map.," *Magnetic Resonance in Medicine*, vol. 37, pp. 457–469, 1997.

[8] Teknomo, Kardi. K-Nearest Neighbors Tutorial. [Online]. Available: http://people.revoledu.com/kardi/tutorial/KNN/.

[9] J. Zhang, K. Ma, M. Er, and V. Chong, "Tumor segmentation from magnetic resonance imaging by learning via one-class support vector machine," in *International Workshop on Advanced Image Technology*, pp. 207–211, 2004.

[10] C. Garcia and J. Moreno, "Kernel based method for segmentation and modeling of magnetic resonance images," *Lecture Notes in Computer Science*, vol. 3315, pp. 636–645, 2004.

[11] P. Gibbs, D. Buckley, S. Blackband, and A. Horsman, "Tumour volume determination from mr images by morphological segmentation," *Physics in Medicine and Biology*, vol. 41, pp. 2437–2446, Nov. 1996.

[12] Y. Zhu and H. Yan, "Computerized tumor boundary detection using a hopfield neural network," *IEEE Transactions on Medical Imaging*, vol. 16, pp. 55–67, 1997.

[13] M. Clark, L. Hall, D. Goldgof, R. Velthuizen, F. Murtagh, and M. Silbiger, "Automatic tumor segmentation using knowledge-based techniques," *IEEE Transactions on Medical Imaging*, vol. 17, pp. 238–251, 1998.

[14] M. Schmidt, "Automatic brain tumor segmentation," Master's thesis, University of Alberta, 2005.

[15] L. Fletcher-Heath, L. Hall, D. Goldgof, and F. R. Murtagh, "Automatic segmentation of non-enhancing brain tumors in magnetic resonance images," *Artificial Intelligence in Medicine*, vol. 21, pp. 43–63, 2001.

[16] S. Shen, W. Sandham, and M. Granat, "Preprocessing and segmentation of brain magnetic resonance images," in *4th International IEEE EMBS Specific Topic Conference on Information Technology Applications in Biomedicine*, pp. 149–152, 2003.

[17] A. Capelle, O. Alata, C. Fernandez, S. Lefevre, and J. Ferrie, "Unsupervised segmentation for automatic detection of brain tumors in mri," in *IEEE International Conference on Image Processing*, 2000.

[18] A. Capelle, O. Colot, and C. Fernandez-Maloigne, "Evidential segmentation scheme of multi-echo mr images for the detection of brain tumors using neighborhood information," *Information Fusion*, vol. 5, no. 3, pp. 203–216, 2004.

[19] A. Evans, D. Collins, and B. Milner, "An mri-based stereotactic atlas from 250 young normal subjects," *Society for Neuroscience Abstracts*, vol. 18, no. 179.4, p. 408, 1992.

[20] A. Evans and D. Collins, "A 305-member mri-based stereotactic atlas for cbf activation studies," *40th Annual Meeting of the Soceity for Nuclear Medicine*, 1993.

[21] Statistical Parametric Mapping, http://www.fil.ion.ucl.ac.uk/spm/.

[22] N. Moon, E. Bullitt, K. Leemput, and G. Gerig, "Automatic brain and tumor segmentation," in *Medical Image Computing and Computer-Assisted Intervention (MICCAI), Springer Verlag*, vol. 2489, pp. 372–379, 2002.

[23] D. Gering, W. Grimson, and R. Kikinis, "Recognizing deviations from normalcy for brain tumor segmentation," in *Medical Image Computing*

and Computer-Assisted Intervention (MICCAI), Springer Verlag, vol. 2488, pp. 388–395, 2002.

[24] J. A. Sethian, *Level Set Methods and Fast Marching Methods : Evolving Interfaces in Geometry, Fluid Mechanics, Computer Vision,and Materials Science.* Cambridge University Press, second ed., 1999.

[25] M. Leventon, W. Grimson, and O. Faugeras, "Statistical shape influence in geodesic active contours," in *CVPR00*, pp. I: 316–323, 2000.

[26] M. Droske, B. Meyer, M. Rumpf, and C. Schaller, "An adaptive level set method for medical image segmentation," in *Proc. of the Annual Symposium on Information Processing in Medical Imaging* (R. Leahy and M. Insana, eds.), Springer, Lecture Notes Computer Science, 2001.

[27] A. Lefohn, J. Cates, and R. Whitaker, "Interactive, gpu-based level sets for 3d brain tumor segmentation," tech. rep., University of Utah, School of Computing Tech., April 2003.

[28] S. Ho, H. Cody, and G. Gerig, "Snap: A software package for user-guided geodesic snake segmentation," tech. rep., University of North Carolina, Chapel Hill, April 2003.

[29] S. Ho, E. Bullitt, and G. Gerig, "Levelset evolution with region competition: Automatic 3d segmentation of brain tumors," in *Proc. of Int'l Conf. on Pattern Recognition*, pp. 532–535, August 2002.

[30] M. Prastawa, E. Bullitt, S. Ho, , and G. Gerig, "A brain tumor segmentation framework based on outlier detection," *Medical Image Analysis*, vol. 8, pp. 275–283, Sep 2004.

[31] T. McInerney and D. Terzopoulos, "Deformable models in medical image analysis: a survey," *Medical Image Analysis*, vol. 1, no. 2, pp. 91–108, 1996.

[32] D. L. Pham, C. Xu, and J. L. Prince, "Current methods in medical image segmentation," *Annual Review of Biomedical Engineering*, vol. 2, p. 315338, 2000.

[33] M. Kass, A. Witkin, and D. Terzopoulos, "Snakes: Active contour models," *International Journal of Computer Vision*, vol. 1, pp. 321–331, Nov. 1988.

[34] Osher, Stanley, Fedkiw, and Ronald, *Level set methods and dynamic implicit surfaces*. Springer, 2003.

[35] A. Mansouri, "Region tracking via level set pdes without motion computation," *PAMI*, vol. 24, pp. 947–961, July 2002.

[36] R. Malladi, J. A. Sethian, and B. C. Vemuri, "Shape modeling with front propagation: A level set approach," *IEEE Trans. on Pattern Analysis and Machine Intelligence*, vol. 17, no. 2, pp. 158–175, 1995.

[37] L. Rudin, S. Osher, and E. Fatemi, "Nonlinear total variation based noise removal algorithm," *Physica D.*, vol. 60, pp. 259–268, 1992.

[38] T. Chan and L. Vese, "Active contours without edges," *IEEE Trans. on Image Processing*, vol. 10, no. 2, pp. 266–277, February 2001.

[39] B. Ostle and L. Malone, *Statistics in research: basic concepts and techniques for research workers*. Iowa State University Press, fourth ed., 1988.

[40] E. W. Weisstein, "Convex (concave)." From MathWorld–A Wolfram Web Resource, [Online]. Available: http://mathworld.wolfram.com/Convex.html.

[41] B. Scholkopf and A. J. Smola, *Learning with kernels: Support vector machines, regularization, optimization, and beyond*. Cambridge: MA: MIT Press, 2002.

[42] V. Vapnik, *The nature of statistical learning theory*. New York: Springer, 1995.

[43] C. Cortes and V. Vapnik, "Support-vector networks," *Machine Learning*, vol. 20, no. 3, pp. 273–297, 1995.

[44] B. Scholkopf, A. Smola, R. Williamson, and P. Bartlett, "New support vector algorithms," *Neural Computation*, vol. 12, no. 5, pp. 1207–1245, 2000.

[45] C. Muller, "Support vector machine based detection of tumours in dynamic mri mammographs," Master's thesis, University of Bielefeld, February 2004.

[46] S. Haykin, *Neural Networks: A Comprehensive Foundation.* Upper Saddle River, NJ: PrenticeHall, 1999.

[47] D. Adalsteinsson and J. Sethian, "A fast level set method for propagating interfaces," *Journal of Computational Physics*, vol. 118, no. 2, pp. 269–277, 1995.

[48] V. Chalana and Y. Kim, "A methodology for evaluation of boundary detection algorithms on medical images," *IEEE Trans. Med. Imaging*, vol. 16, pp. 642–652, 1997.

[49] P. Remiejer, C. Rasch, J. Lebesque, and M. Herk, "A general methodology for three-dimensional analysis of variation in target volume delineation," *Medical Physics*, vol. 26, pp. 931–940, 1999.

[50] K. Vincken, A. Koster, C. De Graaf, and M. Viergever, "Model- based evaluation of image segmentation methods," in *Performance Characterization in Computer Vision*, Kluwer Academic Publishers, 2000.

[51] S. Warfield, K. Zou, and W. Wells, "Validation of image segmentation and expert quality with an expectation-maximization algorithm," in *Medical Image Computing and Computer-Assisted Intervention- MICCAI*, 2002. Tokyo, Japan.

[52] R. Klette, S. Stiehl, M. Viergever, and K. Vincken, *Performance Characterization in Computer Vision*. Kluwer Academic Publishers, 2000.

[53] T. Kapur, E. Grimson, W. Wells, and R. Kikinis, "Segmentation of brain tissue from magnetic resonance images," *Medical Image Analysis*, vol. 1, no. 2, 1996.

[54] G. Gerig, M. Jomier, and M. Chakos, "Valmet: A new validation tool for assessing and improving 3d object segmentation," in *Proc. MICCAI, Springer LNCS 2208*, pp. 516–523, 2001.